THE ASTROPHYSICAL JOURNAL, 457:892–921, 1996 February 1

A NEW SCHEME FOR MULTIDIMENSIONAL LINE TRANSFER. III. A TWO-DIMENSIONAL LAGRANGIAN VARIABLE TENSOR METHOD WITH DISCONTINUOUS FINITE-ELEMENT Sn TRANSPORT

PIETER G. DYKEMA, RICHARD I. KLEIN,[1] AND JOHN I. CASTOR
University of California, Lawrence Livermore National Laboratory, Livermore, CA 94550
Received 1995 February 17; accepted 1995 August 7

ABSTRACT

We describe a new code—ALTAIR—that has been developed to solve the time-dependent non-LTE problem for a multilevel atom in two-dimensional axisymmetric geometry on a Lagrangian mesh of arbitrary complexity. The method and results are presented here for a two-level atom. The extension to a multilevel atom is made by the equivalent two-level atom (ETLA) methods we have recently described in Paper II of this series. The source function of the line formed by the two-level atom is iterated to self-consistency with the radiation field, which is obtained from a system of coupled moment equations that employs an Eddington tensor closure using the double-splitting method described in Paper I of this series. The Eddington tensor itself is derived from a formal solution of the photon transport equation, which is based on a new discontinuous finite-element technique; the tensor moment system uses a continuous representation. The Eddington tensor is updated in an outer iteration loop, within which the double-splitting iteration is used to find the self-consistent source function for a given tensor. The resulting method shows very rapid convergence of the scattering iteration, even for optically thick regions with scattering albedo near unity. In addition, the spatial structure of the solution is rather insensitive to the shape of the spatial zones; the calculation of problems with zone aspect ratios of 1000 to 1 causes no difficulty. Application to several benchmark calculations, including radiative transfer in a nonorthogonal mesh, is discussed. We find that for two-dimensional problems of astrophysical interest, many angle rays are required to ensure an accurate solution.

Subject headings: line formation — methods: numerical — radiative transfer

1. INTRODUCTION

There are now several important astrophysical problems that call for the ability to calculate non-LTE line transport in two spatial dimensions, usually in axisymmetric geometry.[2] We have in mind the calculation of the emission-line spectra of chromospheres and coronae of accretion disks in active galactic nuclei (AGNs) that are irradiated by matter accreting onto supermassive black holes, as well as a study of the spectra of the nonspherical winds from rotating hot stars. We have developed new techniques that treat this problem in some generality. The framework of our approach is described in the first paper of this series (Klein et al. 1989, hereafter Paper I). The method can treat, in a self-consistent manner, time-dependent radiation transport involving a large number of possibly overlapping spectral lines and continua in two spatial dimensions without difficulty. The underlying method we use is an iteration procedure based upon the equivalent two-level atom (ETLA) method. We have recently discussed our modified implementation of this method (Castor, Dykema, & Klein 1992, hereafter Paper II). It is based on iteration of the net radiative brackets (NRBs) corresponding to the various radiative transitions in the atomic system.[3] We thus solve for each line separately, obtaining a radiation field that is consistent with the populations of the upper and lower levels. The fields, in turn, are used to update the transition rates. New estimates of the populations are obtained, and the steps are repeated until the desired level of convergence is achieved. The purpose of the present paper is to describe the two-dimensional transport and acceleration algorithms that we use to solve a given line, and to provide interesting benchmark calculations in two-dimensional x-y and r-z geometry.

The problem of multidimensional line transfer has received increased attention over the last decade, owing to the introduction of supercomputers with sufficient memory and speed to perform the required calculations. Early work in this area includes the papers of Cannon & Rees (1971), who used a generalized Feautrier (1964) technique and the improvement on this approach developed by Mihalas, Auer, & Mihalas (1978), who employed a Rybicki (1971) elimination scheme. More recent work in multidimensional line transport is that of Kunasz & Olson (1988) and an attempt to treat three-dimensional problems by Nordlund (1991).

Although several papers have appeared in the astrophysics literature on the subject of two-dimensional line transfer, there is relatively little in the way of techniques that can be applied to the solution of problems in which both a large number of zones is required to resolve structures of interest and there are many spectral lines, angles, and frequencies to consider, with a correspondingly large number of atomic levels. Furthermore, time dependence must be considered. In anticipation of astrophysical problems of such complexity, we believe that for the first time we have developed an approach to multidimensional line and continuum radiation transport that has several new features incorporated together. Our time-dependent code, which has both one-dimensional and two-dimensional capability, is called ALTAIR.

[1] Also Berkeley Department of Astronomy and the Theoretical Astrophysics Center, University of California at Berkeley.

[2] Non-LTE refers to problems in which the radiation field in some number of lines and photoionization continua depends, through the absorption and emission coefficients, on a set of atomic level populations, which depend in turn on the rates of photon processes involving the same radiation field; thus the radiation field and the level populations must be found self-consistently.

[3] The NRB is a form factor, z, relating the mean intensity in a line or continuum to the source function: $z = 1 - \bar{J}/S$.

The phase space for the photon distribution in a two-dimensional spatial domain is actually a six-dimensional spacetime (2 space, 2 angle, 1 frequency, and 1 time). Thus, the size of the finite-difference system representing the partial differential equations is enormous, even for problems of modest scale. For problems involving resonance-line scattering, direct solutions, such as those proposed in earlier work, are clearly prohibitive; thus, we have opted for a multilayered iterative approach involving the ETLA iteration described in detail in Paper II, combined with the new double-splitting iterative solution of the coupled tensor radiation moment equations that we introduced in Paper I, which lies at the core of our approach. We showed in Paper I that our new iterative splitting approach is as good as or better than any of the currently available operator perturbation techniques and, in our opinion, represents the best way to do multidimensional line transport. We have developed our formalism to include both axisymmetric (cylindrical r-z) geometry and planar x-y geometry. We have allowed for different regions of the plasma to have different compositions. In a dynamical calculation, the interface between materials can become highly distorted, hence we have developed the difference schemes on a Lagrangian mesh, that is, a logically rectangular mesh for which the grid lines are fixed relative to the fluid, which ensures that material interfaces always coincide with grid lines. This is the first time this has been accomplished for multidimensional transport. Alternatively, we can easily run Eulerian grid calculations using a straightforward remap procedure. We have previously reported preliminary results in Castor, Dykema, & Klein (1991). Here we discuss the complete formuation of the problem.

For problems in which the conditions in the gas vary significantly on the light-transit timescale, the radiation field cannot respond instantaneously to changes in the plasma, and itself becomes a dynamical entity (Mihalas & Mihalas 1984). Accordingly, we have developed ALTAIR to include the retardation effect for the radiation field, as well as time dependence of the atomic level populations. In addition, certain phenomena may require a large zone-to-zone variation in fundamental quantities, such as temperature, density, and opacity, that can directly affect the line transport. Thus, we have developed radiative transport schemes that do not assume that such quantities have smooth spatial variation. We have been able to handle problems with large dynamic ranges in the properties of the medium, while retaining accuracy and stability. We will demonstrate that our approach is robust, stable, and convergent, and is accurate in situations in which spatial and temporal structures are reasonably well resolved.

Our algorithm for solving the two-level atom line-scattering problem proceeds as follows. From estimates of the opacity and source function for the line, we obtain a formal solution for the radiation intensity by solving the photon transport equation in first-order form. The source function, which is not varied during the formal solution procedure, contains a contribution from the line-scattering integral that is itself a function of the radiation field. If the line is optically thin, or if the source function is collisionally dominated, it may suffice in the iteration procedure simply to reconstitute the scattering integral from the formal solution intensities. The result would then be used in the next formal solution for the line in the next ETLA iteration. However, if the line is thick and scattering-dominated, this lambda iteration will converge too slowly to be of practical value, and means must be found to accelerate the convergence of the scattering integral. We require a guess at the radiation energy density, as a function of frequency within the line, that does not depend strongly on the angular structure of the radiation field. We obtain such a guess by solving the system stress-energy equations. These equations, which govern the exchange of energy and momentum between photons and material, may be obtained formally as the zeroth and first angular moments of the photon transport equation. The moment equations are closed at the second-moment level by considering the photon-pressure tensor to be the product of the photon energy density, an unknown, and a dimensionless Eddington tensor, which is obtained from the just computed formal solution. The idea behind the scheme is that the Eddington tensor, being a ratio, will vary less during the iteration procedure than will the radiation pressure and the energy density separately. We then expect that the energy densities that we obtain as the solution to the moment equations can be used in the formal solution to construct a good advanced guess at the scattering integral for the next ETLA iteration. This expectation has been realized in every calculation we have made to data. The procedure appears to be stable and rapidly convergent. Our method is a generalization to two dimensions of the variable Eddington factor method developed in one dimension by Auer & Mihalas (1970). This method has been described by Goldin (1964), who calls it quasi diffusion, in the context of neutron-scattering problems.

The structure of our paper is as follows. In § 2, we develop the tensor moment equations directly from the radiation transport equation in r-z geometry. We show how the moment equations are naturally combined to form a second-order equation by implicit differencing of the time operator as in Mihalas & Klein (1982). We display the combined tensor moment equations in both vector operator and component form.

In § 3 we discuss the discrete representation of the radiation transport equations on the numerical grid, which is a logically rectangular mesh of convex quadrilateral zones. To solve the transport equation, we use a modified discontinuous fine-element (DFE) technique. DFE schemes have been used for many years in neutron transport codes (Mordant 1975, 1976, 1981). As a group, they differ from continuous schemes by allowing the approximate solution to exhibit jump discontinuities across zone interfaces. As one might expect, DFE algorithms tend to be quite stable under conditions of large zone-to-zone variation in sources and opacities—condition which, we have noted, we expect to encounter. Our modification of an otherwise consistent method is simply to "mass lump" the time evolution, emission, and absorption terms, i.e., to diagonalize, with respect to these terms, the matrix that must be inverted in each zone to obtain the approximate solution. This renders the scheme even more stable.

In § 4 we discuss the discretization of the moment equations, which, in contrast to the transport equations, incorporates the assumption that the energy-density field that is the solution to these equations is, in fact, continuous across zone interfaces. We therefore have the situation where the moment equations are analytically consistent with the transport equation, having been derived from it by angle quadratures, but the same cannot be said of the numerical moment scheme, which is manifestly inconsistent with the numerical transport algorithm. This inconsistency is known to cause stability problems in certain linear acceleration methods. In the variable Eddington tensor method, which, incidentally, is nonlinear because of the closure in terms of the Eddington tensor times energy density, we observe no sign of instability, though we have no proof to offer that the scheme is unconditionally stable. What we do observe is some small disagreement between the transport and the moment energies at convergence, with the

difference lessening as the zoning becomes finer. We then show a completely self-consistent formulation of the moment equations with the radiation transport equation for which exact agreement of the transport and moment energies is ensured. Finally, we describe the sequence of steps necessary for the solution of the moment equations.

In § 5 we describe four applications of the method of this paper to steady state two-dimensional line-scattering problems. These are as follows (1) an infinitely long rectagular prism in x-y geometry, within which all the line and continuum properties are constant; (2) a nonuniform source problem—a square prism as in application 1, but with the Planck function following a Gaussian distribution with distance away from the diagonal of the square; (3) a problem with a sharp material boundary—a rectangular prism of perfectly absorbing cold material embedded in a larger rectangular prism of less opaque emitting material, the so-called Mordant test problem (after Mordant 1981); and (4) line formation in a cylinder. The conclusions of this work are summarized in § 6. Future papers in this series will introduce a new angle multigrid perturbation method for two-dimensional line transport, with applications to rotating accretion disks associated with AGNs and X-ray binaries.

2. VARIABLE TENSOR MOMENT EQUATIONS

2.1. *The Transport Equation*

We begin by introducing the radiation transport equation in lines and continua (cf. Paper I):

$$\frac{1}{c}\frac{\partial I_\nu}{\partial t} + \boldsymbol{\Omega}\cdot\nabla I_\nu(\boldsymbol{\Omega}) = -(\chi_c + \chi_l\Phi_\nu)I_\nu + \chi_c S_c + \chi_l\Phi_\nu S_\nu\,, \tag{2.1}$$

where $\eta_c \equiv \chi_c S_c$ is the continuum emissivity, $\eta_l \equiv \chi_l S_\nu$ is the line emissivity, Φ_ν is the profile function in the line, and $\boldsymbol{\Omega}$ is the unit direction vector.

Assuming a cylindrical geometry with azimuthal symmetry and coordinates r, z, and ϕ, we note that the specific intensity is a six-dimensinal phase space dependent upon t, ν, $\boldsymbol{\Omega}$, r and z, where the unit direction vector is

$$\boldsymbol{\Omega} = \Omega^r\boldsymbol{e}_r + \Omega^z\boldsymbol{e}_z + \Omega^\phi\boldsymbol{e}_\phi \tag{2.2}$$

in terms of its components

$$\Omega^r = \sin\theta\cos\psi\,, \qquad \Omega^z = \cos\theta\,, \qquad \Omega^\phi = \sin\theta\sin\psi\,. \tag{2.3}$$

Here θ is the polar angle measured from the positive z-direction, ψ is the local azimuthal angle such that $\psi = 0$ designates the local positive r-direction, and ϕ is the global azimuthal angle about the z-axis. If we assume axial symmetry, $\partial I/\partial\phi = 0$, the transport equation (2.1) becomes

$$\frac{1}{c}\frac{\partial I_\nu}{\partial t} + \cos\theta\frac{\partial I_\nu}{\partial z} + \frac{\sin\theta\cos\psi}{r}\frac{\partial}{\partial r}(rI_\nu) - \frac{\sin\theta}{r}\frac{\partial}{\partial\psi}(\sin\psi I_\nu) = -(\chi_c + \chi_l\Phi_\nu)I_\nu + \chi_c S_c + \chi_l\Phi_\nu S_\nu\,. \tag{2.4}$$

2.2. *Moments of the Radiation Field*

We next develop zeroth and first-moment equations of the transport equation by integrating it against solid angle $d\omega$ and $\boldsymbol{\Omega}\,d\omega$. We obtain for the moment at all spatial points (r, z) the mean intensity

$$J_\nu = \frac{1}{4\pi}\oint d\omega\, I_\nu(\boldsymbol{\Omega})\,, \tag{2.5}$$

the Eddington flux

$$\boldsymbol{H}_\nu = \frac{1}{4\pi}\oint d\omega\,\boldsymbol{\Omega} I_\nu(\boldsymbol{\Omega})\,, \tag{2.6}$$

and the second moment

$$\boldsymbol{K}_\nu = \frac{1}{4\pi}\oint d\omega\,\boldsymbol{\Omega}\boldsymbol{\Omega} I_\nu(\boldsymbol{\Omega})\,, \tag{2.7}$$

where $\boldsymbol{H}_\nu$ and $\boldsymbol{K}_\nu$ are understood to be second-rank tensors.

In component form, we find for the Eddington flux

$$H_r = \frac{1}{4\pi}\oint \sin\theta\cos\psi\, I_\nu(\boldsymbol{\Omega})d\omega\,, \tag{2.8}$$

$$H_z = \frac{1}{4\pi}\oint \cos\theta\, I_\nu(\boldsymbol{\Omega})d\omega\,, \tag{2.9}$$

$$H_\phi = \frac{1}{4\pi}\oint \sin\theta\sin\psi\, I_\nu(\boldsymbol{\Omega})d\omega = 0\,, \tag{2.10}$$

and for components of the second moment,

$$K_{rr} = \frac{1}{4\pi} \oint \sin^2 \theta \cos^2 \psi \, I_\nu(\Omega) d\omega \,, \tag{2.11}$$

$$K_{rz} = \frac{1}{4\pi} \oint \cos \theta \sin \theta \cos \psi \, I_\nu(\Omega) d\omega \,, \tag{2.12}$$

$$K_{r\phi} = \frac{1}{4\pi} \oint \sin^2 \theta \sin \psi \cos \psi \, I_\nu(\Omega) d\omega = 0 \,, \tag{2.13}$$

$$K_{\phi\phi} = \frac{1}{4\pi} \oint \sin^2 \theta \sin^2 \psi \, I_\nu(\Omega) d\omega \,, \tag{2.14}$$

$$K_{zz} = \frac{1}{4\pi} \oint \cos^2 \theta \, I_\nu(\Omega) d\omega \,, \tag{2.15}$$

and

$$K_{\phi z} = \frac{1}{4\pi} \oint \cos \theta \sin \theta \sin \psi \, I_\nu(\Omega) d\omega = 0 \,. \tag{2.16}$$

(H_ϕ, $K_{r\phi}$, and $K_{\phi z}$ vanish because I_ν is an even function of ψ for axial symmetry.)

2.3. *Tensor Moment Equations*

If we make the assumption that the velocity field vanishes (we will present results for nonzero velocity fields in a subsequent paper), the zeroth-moment equation is obtained by integrating equation (2.4) over $d\omega$.

$$\frac{1}{c}\frac{\partial J}{\partial t} + \frac{1}{r}\frac{\partial}{\partial r}(rH_r) + \frac{\partial H_z}{\partial z} = \chi_c S_c + \chi_l S_\nu \Phi_\nu - (\chi_c + \chi_l \Phi_\nu) J \,, \tag{2.17}$$

where we have dropped frequency subscripts on radiation field quantities for convenience. Similarly, if we integrate equation (2.4) over $\Omega_r \, d\omega$, we obtain

$$\frac{1}{c}\frac{\partial H_r}{\partial t} + \frac{1}{r}\frac{\partial}{\partial r}(rK_{rr}) + \frac{\partial K_{rz}}{\partial z} - \frac{J - K_{rz} - K_{zz}}{r} = -\chi_c H_r - \chi_l \Phi_\nu H_r \,. \tag{2.18}$$

In deriving equation (2.18), we made use of the trace condition on the second moment $\boldsymbol{K}$,

$$K_{rr} + K_{zz} + K_{\phi\phi} = J \,, \tag{2.19}$$

to eliminate $K_{\phi\phi}$ in terms of K_{rr} and K_{zz}. Integrating equation (2.4) over $\Omega_z \, d\omega$ gives

$$\frac{1}{c}\frac{\partial H_z}{\partial t} + \frac{1}{r}\frac{\partial}{\partial r}(rK_{rz}) + \frac{\partial K_{zz}}{\partial z} = -\chi_c H_z - \chi_l \Phi_\nu H_z \,. \tag{2.20}$$

We note that to within a factor $c/4\pi$, equation (2.17) is the radiation energy equation, and equations (2.18) and (2.20) are the radial and axial components of the radiation momentum equation.

In order to close the moment equations (2.17), (2.18), and (2.20), we now define a variable Eddington tensor:

$$\boldsymbol{T}_\nu \equiv \frac{\boldsymbol{K}_\nu}{J_\nu} = \frac{\oint d\omega \, \Omega\Omega \, I_\nu(\Omega)}{\oint d\omega \, I_\nu(\Omega)} \,, \tag{2.21}$$

and the two components of the first-moment equation become

$$\frac{1}{c}\frac{\partial H_r}{\partial t} + \frac{1}{r}\frac{\partial}{\partial r}(rT_{rr} J) + \frac{\partial}{\partial z}(T_{rz} J) - \frac{1 - T_{rr} - T_{zz}}{r} J = -\chi_c H_r - \chi_l \Phi_\nu H_r \tag{2.22}$$

and

$$\frac{1}{c}\frac{\partial H_z}{\partial t} + \frac{1}{r}\frac{\partial}{\partial r}(rT_{rz} J) + \frac{\partial}{\partial z}(T_{zz} J) = -\chi_c H_z - \chi_l \Phi_\nu H_z \,. \tag{2.23}$$

Thus, equations (2.17), (2.22), and (2.23) complete the set of tensor moment equations whose solution for J we seek upon specification of the T_{rr}, T_{rz}, and T_{zz} components of the Eddington tensor, in addition to the sources and sinks.

2.4. *Combined Tensor Moment Equation*

The combined moment equation was derived in Paper I, where the discussion was given in general vector form. We recall that discussion here. Equation (2.17) is written

$$\frac{1}{c}\frac{\partial J_\nu}{\partial t} + \nabla \cdot \boldsymbol{H}_\nu = \chi_c S_c + \chi_l S_\nu \Phi_\nu - (\chi_c + \chi_l \Phi_\nu) J_\nu , \tag{2.24}$$

and similarly for equations (2.22) and (2.23)

$$\frac{1}{c}\frac{\partial \boldsymbol{H}_\nu}{\partial t} + \nabla \cdot (\boldsymbol{T}_\nu J_\nu) = -\chi_c \boldsymbol{H}_\nu - \chi_l \Phi_\nu \boldsymbol{H}_\nu . \tag{2.25}$$

These equations can be combined by eliminating $\boldsymbol{H}_\nu$ after using backward time differencing to replace the derivative on the left-hand-side of equation (2.25) with $(\boldsymbol{H}_\nu - \boldsymbol{H}_\nu^0)/\Delta t$:

$$\frac{1}{c}\frac{\partial J_\nu}{\partial t} - \nabla \cdot \left[\frac{1}{1/(c\Delta t) + \chi_c + \chi_1 \Phi_\nu} \nabla \cdot (\boldsymbol{T}_\nu J_\nu) - \frac{\boldsymbol{H}_\nu^0}{1 + c\Delta t(\chi_c + \chi_1 \Phi_\nu)} \right] = \chi_c S_c + \chi_1 S_\nu \Phi_\nu - (\chi_c + \chi_1 \Phi_\nu) J_\nu \tag{2.26}$$

(cf. Paper I, eq. [8]). All quantities are at the current time t, except $\boldsymbol{H}_\nu^0$, which is defined at $t - \Delta t$.

We employ a variable Eddington tensor iteration method to solve equation (2.26) simultaneously with the atomic kinetics (rate equations) that determine atomic populations necessary to obtain x_l and η_l, etc. We note that the mean intensity J_ν in a given frequency is coupled to J_ν in all other frequencies (over all lines) through the implicit dependence of η_l, etc., on J_ν that results from the existence of radiative rate terms in the rate equations. To simplify the coupling of the radiation fields, we introduce the ETLA source function relation for the transition between levels l and u. We express the line source function as

$$S_\nu = \gamma_\nu \bar{J} + \epsilon_\nu , \tag{2.27}$$

in which γ_ν and ϵ_ν are algebraic combinations of the rates coupling levels l and u to all other levels and of the collisional rates connecting level l to level u, and $\bar{J}$ is the frequency scattering integral for the transition l–u (cf. Mihalas 1978 and Paper II). We use the current values for all the coefficients (γ_ν, ϵ_ν, etc.), but $\bar{J}$ in equation (2.27) is expressed in terms of the to-be-found J_ν. We thus obtain the combined moment equation as in Paper I:

$$\frac{1}{c}\frac{\partial J_\nu}{\partial t} - \nabla \cdot \left[\zeta \nabla \cdot (\boldsymbol{T}_\nu J_\nu) - \frac{\zeta}{c\Delta t} \boldsymbol{H}_\nu^0 \right] = \chi_c S_c + \chi_l \Phi_\nu \gamma_\nu \bar{J} + \epsilon_\nu - (\chi_c + \chi_l \Phi_\nu) J_\nu , \tag{2.28}$$

where

$$\zeta = [1/(c\Delta t) + \chi_c + \chi_l \Phi_\nu]^{-1} .$$

The moment equations are now frequency-coupled, but only within a particular transition, through $\bar{J}$. They are linear in J_ν and can be solved in parallel on a line-by-line basis. The coefficients γ_ν and ϵ_ν depend upon the radiative and collisional interactions of levels l and u with all other levels, and are updated in the ETLA iteration loop (cf. Paper II).

Let us consider the combined moment equation (2.28) in full component form in cylindrical two-dimensional geometry. We first use fully implicit time differencing in equations (2.22) and (2.23) to obtain the radial and axial components of the radiation flux,

$$H_r^{n+1} = \frac{\zeta^{n+1} H_r^n}{c\Delta t} - \zeta^{n+1} \frac{1}{r}\frac{\partial}{\partial r}(r T_{rr} J^{n+1}) - \zeta^{n+1} \frac{\partial}{\partial z}(T_{rz} J^{n+1}) + \frac{\zeta^{n+1}}{r}(1 - T_{rr} - T_{zz}) J^{n+1} \tag{2.29}$$

and

$$H_z^{n+1} = \frac{\zeta^{n+1}}{c\Delta t} H_z^n - \frac{\zeta^{n+1}}{r}\frac{\partial}{\partial r}(r T_{rz} J^{n+1}) - \zeta^{n+1} \frac{\partial}{\partial z}(T_{zz} J^{n+1}) . \tag{2.30}$$

We note that all quantities with superscript $n + 1$ are defined at the advanced time, and quantities with superscript n are defined at the past time.

We now substitute equations (2.29) and (2.30) in a backward time-differenced form of equation (2.27) to obtain the time-differenced, combined tensor moment equations for J_ν:

$$\begin{aligned} J_\nu^{n+1} &- \frac{\zeta^{n+1}}{r}\frac{\partial}{\partial r}\left[\zeta^{n+1} \frac{\partial}{\partial r}(r T_{rr} J_\nu^{n+1}) \right] - \frac{\zeta^{n+1}}{r}\frac{\partial}{\partial r}\left[\zeta^{n+1} r \frac{\partial}{\partial z}(T_{rz} J_\nu^{n+1}) \right] \\ &+ \frac{\zeta^{n+1}}{r}\left[\frac{\partial}{\partial r} \zeta^{n+1}(1 - T_{rr} - T_{zz}) J_\nu^{n+1} \right] - \zeta^{n+1}\frac{\partial}{\partial z}\left[\frac{\zeta^{n+1}}{r}\frac{\partial}{\partial r}(r T_{rz} J_\nu^{n+1}) \right] - \zeta^{n+1}\frac{\partial}{\partial z}\left[\zeta^{n+1}\frac{\partial}{\partial z}(T_{zz} J_\nu^{n+1}) \right] \\ &= -\frac{\zeta^{n+1}}{c\Delta t}\frac{1}{r}\frac{\partial}{\partial r}(r \zeta^{n+1} H_{vr}^n) - \frac{\zeta^{n+1}}{c\Delta t}\frac{\partial}{\partial z}(\zeta^{n+1} H_{vz}^n) + \zeta^{n+1}\eta_c + \zeta^{n+1}\Phi_\nu \chi_l(\gamma_\nu \bar{J}^{n+1} + \epsilon_\nu) + \frac{\zeta^{n+1}}{c\Delta t} J_\nu^n . \end{aligned} \tag{2.31}$$

We note that equation (2.31) goes correctly to the diffusion and wavelike limits as $c\Delta t\chi$ approaches ∞ and 0, respectively. We have

assumed, in using the ETLA source function in equation (2.31), that the line transition is formed in complete redistribution. The generalization to partial redistribution is straightforward and presents no difficulties, as we have shown in Paper I. Multidimensional calculations with partial redistribution (PRD) will be reported in future papers.

2.5. *Boundary Conditions for the Moment Equations*

We require the boundary condition for the combined tensor moment equation. There are two distinct physical boundary conditions that we may wish to apply to the radiation field. The first is a specification of the incoming intensity. The second is a reflection or symmetry condition, which takes the simple form $\boldsymbol{H} = 0$. One or the other of these two conditions is to be applied at any point on the boundary ∂R of the solution domain. For the combined moment equation, the boundary condition must be expressed as a relation between $\boldsymbol{H}$ and J. Clearly, the reflection condition is already in that form. To express the incoming intensity constraint in that form we proceed as follows. Define the hemisphere fluxes $\boldsymbol{H}^+$ and $\boldsymbol{H}^-$ on ∂R to be

$$\boldsymbol{H}^+ = \frac{1}{4\pi}\int_{\hat{\boldsymbol{\Omega}}\cdot\hat{\boldsymbol{n}}>0} d\omega\,\hat{\boldsymbol{\Omega}} I\,, \qquad \boldsymbol{H}^- = \frac{1}{4\pi}\int_{\hat{\boldsymbol{\Omega}}\cdot\hat{\boldsymbol{n}}<0} d\omega\,\hat{\boldsymbol{\Omega}} I\,, \tag{2.32}$$

and the hemisphere mean intensities as

$$J^+ = \frac{1}{4\pi}\int_{\hat{\boldsymbol{\Omega}}\cdot\hat{\boldsymbol{n}}>0} d\omega\, I$$

and

$$J^- = \frac{1}{4\pi}\int_{\hat{\boldsymbol{\Omega}}\cdot\hat{\boldsymbol{n}}<0} d\omega\, I\,.$$

We manipulate the expression for the normal component of the flux in the following way:

$$\boldsymbol{H}\cdot\hat{\boldsymbol{n}} = \boldsymbol{H}^+\cdot\hat{\boldsymbol{n}} + \boldsymbol{H}^-\cdot\hat{\boldsymbol{n}} = \frac{\boldsymbol{H}^+}{J^+}(J - J^-)\cdot\hat{\boldsymbol{n}} + \boldsymbol{H}^-\cdot\hat{\boldsymbol{n}} \equiv \beta(J - J^-) + \boldsymbol{H}^-\cdot\hat{\boldsymbol{n}}\,, \tag{2.33}$$

where

$$\beta = \frac{\boldsymbol{H}^+\cdot\hat{\boldsymbol{n}}}{J^+} \tag{2.34}$$

is the boundary Eddington factor and $\hat{\boldsymbol{n}}$ is directed outward from R. The incoming hemisphere terms J^- and $\boldsymbol{H}^-\cdot\hat{\boldsymbol{n}}$ are determined from the specified incident intensity that provides the boundary condition for the solution of the transport equation (2.1). The boundary Eddington factor is computed from the solution of this equation.

3. NUMERICAL DISCRETIZATION OF THE TRANSPORT EQUATION

The transport equation (2.1) is used to construct the Eddington tensor components (eqs. [2.11]–[2.16]) and the boundary Eddington factor (eq. [2.34]) that close the combined tensor moment equation (2.31). Here we discuss the discontinuous finite-element representation of equation (2.1).

3.1. *Bilinear Quadrilateral Element Representation of Intensity*

The problem of obtaining accurate numerical solutions to the photon transport equation is exacerbated in multidimensional calculations by the use of nonorthogonal numerical grids, where interpolation polynomial techniques become difficult to apply, and by the presence of large zone-to-zone variations in the composition and state of the medium. Our approach to the solution of these problems has been to modify discontinuous finite elements (DFE), a technique used in neutron transport (Mordant 1981). The underlying philosophy of the technique is to a priori restrict the approximate numerical solution of the discretized transport equation to a particular function space on a specified region of the solution domain R. The specified region defines a zone, and the parameterized function defines a finite element on the zone. The parameters of the function represent the degrees of freedom of the specific intensity, and the transport equation is solved when these parameters have been determined. The power and flexibility of this approach is greatly enhanced in the case of the transport equation when one relaxes the requirement that contiguous elements need be continuous across their interface. The picture that emerges is of an intensity field exhibiting nontrivial but differentiable structure within each zone, with jump discontinuities across zone interfaces. Application of the transport operator yields regular terms that represent flow within a zone and delta-function type singular terms on zone boundaries that, when properly interpreted, give the zone-to-zone flux. The effect is to break the global solution procedure into a sequence of Galerkin problems, one for each zone.

We assume that the approximate solution is contained in the space of bilinear shape functions for every zone. The properties of these functions are given in Appendix B. For each individual zone we have a map like equation (B1) that allows us to write a formal expansion for the intensity in terms of its vertex values:

$$I(r, z) = \sum_{l=1}^{4} w_l(r, z) I_l\,. \tag{3.1}$$

The global structure of the solution is then that of equation (3.1) within each zone, but with jump discontinuities across zone interfaces. In forming the finite-element equations, we perform surface integrals over the boundaries of the zones, and so we require a unique value for the intensity on the interfaces; for this we choose the value obtained in the limit as the interface is approached in the ray direction $\hat{\Omega}$, that is, the value on the upwind side of the boundary. The discontinuity is then considered to occur on the downwind side. This *Ansatz* will ensure that information is passed in the direction of $\hat{\Omega}$ through the grid. It is perhaps worth emphasizing that this treatment of the boundary terms is physically motivated and does not follow from any more fundamental mathematical property of the DFE technique. A similar issue arises in the treatment of the flux divergence (eq. [4.11]) for the combined tensor moment equation and is resolved differently.

We describe the spatial discretization of equation (2.1) by writing it in schematic form as

$$\frac{1}{c}\frac{\partial I}{\partial t} + \hat{\Omega}\cdot\nabla I = \eta - \chi I \,, \tag{3.2}$$

where η is the total emissivity, χ is the total opacity, and we have dropped the frequency subscripts. Also missing from equation (3.2) is the explicit representation of the "angle transport" term shown in equation (2.4). It is treated below in the detailed dsicussion of § 3.3. First, however, we consider the more generic aspects of the DFE technique as implemented in ALTAIR. We use a discrete ordinates approximation, wherein the unit sphere is partitioned into solid angle bins, each characterized by a mean ray direction $\hat{\Omega}$. The solution procedure is explicit. Thus, given a direction $\hat{\Omega}$, a topological ordering algorithm orders the zones from upwind to downwind, starting on the upwind boundary of the solution domain. The zones are then solved in order. For each zone the four unknown coefficients I_l must be determined simultaneously. We generate four equations from equation (3.2) by multiplying by four linearly independent test functions and integrating over the volume of the zone. We use as test functions the Lagrange basis functions (eq. [B2]), although any set of four linearly independent functions that span the space will suffice for the canonical procedure. When the approximate solution in equation (3.1) is differentiated in equation (3.2), we pick up a regular term in the interior of the zone plus delta-function singularities on the zone boundaries, where the strength of the singularity is given by the difference of the approximate solution across the boundary. Employing the *Ansatz* that only upwind boundary singularities contribute, we obtain the following set of equations:

$$\sum_{k=1}^{4}\left[\left(\frac{\partial I_k}{\partial t} + \chi I_k - \eta_k\right)\int dV\, w_l w_k + I_k\hat{\Omega}\cdot\int dV\, w_l \nabla w_k - (I_k - I_k^*)\int_{\partial^- V} dA\, w_l w_k \hat{\Omega}\cdot\hat{n}\right] = 0 \,, \tag{3.3}$$

$l = 1, 2, 3, 4$. Here V is the volume of revolution of the quadrilateral zone, $\hat{n}$ is the outwardly point unit normal vector on the zone boundary, and $\partial^- V$ is the visible, or upwind, part of the boundary, characterized by $\hat{\Omega}\cdot\hat{n} < 0$. I^* is the approximate solution on the upwind side of $\partial^- V$. It was obtained earlier in the sweep through zones and is therefore a known source term in equations (3.3).

It is straightforward to show that I_k does not contribute to the flow across the upwind boundary. An integration by parts gives

$$\hat{\Omega}\cdot\int dV\, w_l \nabla w_k = \int_{\partial V} dA\, w_l w_k \hat{\Omega}\cdot\hat{n} - \hat{\Omega}\cdot\int dV\, w_k \nabla w_l \,, \tag{3.4}$$

so that equation (3.3) becomes

$$\sum_{k=1}^{4}\left[\left(\frac{1}{c}\frac{\partial I_k}{\partial t} + \chi I_k - \eta_k\right)\int dV\, w_l w_k - I_k\hat{\Omega}\cdot\int dV\, w_k \nabla w_l + I_k\int_{\partial^+ V} dA\, w_l w_k \hat{\Omega}\cdot\hat{n} + I_k^*\int_{\partial^- V} dA\, w_l w_k \hat{\Omega}\cdot\hat{n}\right] = 0 \,, \tag{3.5}$$

$l = 1, 2, 3, 4$, where $\partial^+ V$ is the downwind part of the boundary, characterized by $\hat{\Omega}\cdot\hat{n} > 0$. Equation (3.5) shows the boundary flows explicitly. The ∇w_l term in the equation can be considered to describe flows interior to the zone, a picture that is reinforced when equation (3.5) is summed on l. Using equation (B4), so that

$$\Delta\sum_{l=1}^{4} w_l = 0 \,, \tag{3.6}$$

we obtain

$$\int dV\left(\frac{1}{c}\frac{\partial I}{\partial t} + \chi I - \eta\right) + \int_{\partial^+ V} dA\, I\hat{\Omega}\cdot\hat{n} + \int_{\partial^- V} dA\, I^*\hat{\Omega}\cdot\hat{n} = 0 \,. \tag{3.7}$$

The volume integral of I changes in the time only in response to sources, sinks, and flows across the volume boundaries.

Equation (3.5) exhibit the property that the emission, absorption, and time evolution terms in the lth equation contain contributions from all four intensity degrees of freedom on the zone. We decouple these terms by applying "mass lumping" (discussed in detail in § 4.3),

$$\int dV\, w_l w_k \to \delta_{kl}\int dV\, w_l \,, \tag{3.8}$$

after which equations (3.5) takes the form

$$\left(\frac{1}{c}\frac{\partial I_l}{\partial t} + \chi I - \eta_l\right)V_l + \sum_{k=1}^{4}\left(-I_k\hat{\Omega}\cdot\int dV\, w_k\nabla w_l + I_k\int_{\partial^+ V} dA\, w_l w_k\hat{\Omega}\cdot\hat{n} + I_k^*\int_{\partial^- V} dA\, w_l w_k\hat{\Omega}\cdot\hat{n}\right) = 0 \,, \tag{3.9}$$

$l = 1, 2, 3, 4$, where

$$V_l = \int dV\, w_l \tag{3.10}$$

is the volume of the quadrilateral zone associated with the lth degree of freedom on that zone. The reason for making the substitution in equation (3.8) is again that the robustness of the algorithm is substantially increased. The reduction of equation (3.9) to the case of linear elements in one spatial dimension yields, by inspection, the results that the scheme is very nearly positive, and that the mean intensity constructed in any physically reasonable way is strictly positive, properties not shared by equation (3.5). For the case of radiation flow through a pure absorption medium, equation (3.9) tends to underestimate the exponential falloff, while equation (3.5) errs by overestimating it.

When represented in terms of cylindrical coordinates, the radiation transport equation can be written in the conservative form of equation (2.4), characterized by the property that the angle transport term vanishes identically when integrated over solid angle, leaving a conservative spatial differencing of the flux divergence. This equation is discretized according to equation (3.9), augmented by an angle transport contribution:

$$\left(\frac{1}{c}\frac{\partial I_l}{\partial t} + \chi I_l - \eta_l\right)V_l + \sum_{k=1}^{4}\left[-\cos\theta\, I_k \int dV\, w_k \frac{\partial}{\partial z} w_l - \sin\theta\cos\psi\, I_k \int dV\, w_k \frac{\partial}{\partial r} w_l - \sin\theta \frac{\partial}{\partial \psi}\left(\sin\psi\, I_k \int dV \frac{w_k w_l}{r}\right)\right.$$
$$\left. + I_k \int_{\partial^+ V} dA\, w_l w_k(\cos\theta\, \hat{\boldsymbol{n}}^z + \sin\theta\cos\psi\, \hat{\boldsymbol{n}}^r) + I_k^* \int_{\partial^- V} dA\, w_l w_k(\cos\theta\, \hat{\boldsymbol{n}}^z + \sin\theta\cos\psi\, \hat{\boldsymbol{n}}^r)\right] = 0 . \tag{3.11}$$

The matrix elements of equation (3.11) are evaluated first by transforming to local coordinates and then performing the indicated integrations.

The z derivative in equation (3.11) can be written, using the derivative expressions in Appendix B, as

$$(I\,\partial_z w_l) = \sum_{k=1}^{4} I_k \int dV\, w_k \frac{\partial}{\partial z} w_l = 2\pi \int\int_0^1 d\alpha\, d\beta (f_r g_z - f_z g_r) r I \frac{\partial w_l}{\partial z} .$$

From equation (B13) we obtain

$$\frac{\partial w_l}{\partial z} = \frac{f_r g_{w_l} - f_{w_l} g_r}{f_r g_z - f_z g_r} ,$$

so that

$$(I\,\partial_z w_l) = 2\pi \int\int_0^1 d\alpha\, d\beta (f_r g_{w_l} - f_{w_l} g_r) r I . \tag{3.12}$$

This can be evaluated in terms of equation (B17) by letting $G = r$, $H = I$, and by modifying the Jacobian through the replacement of z by w_l. Similarly, we find

$$(I\,\partial_r w_l) = \sum_{k-1}^{4} I_k \int dV\, w_k \frac{\partial w_l}{\partial z} = 2\pi \int\int_0^1 d\alpha\, d\beta (f_{w_l} g_z - f_z g_{w_l}) r I . \tag{3.13}$$

The remaining volume integrals in equation (3.11) come from the angle transport term. They are of the form

$$\left(\frac{I w_l}{r}\right) = \sum_{k=1}^{4} I_k \int dV \frac{w_k w_l}{r} = 2\pi \int\int_0^1 d\alpha\, d\beta (f_r g_z - f_z g_r) I w_l , \tag{3.14}$$

and follow from equation (B17), with $G = I$ and $H = w_l$. Explicit evaluations of the volume of revolution and equations (3.12)–(3.14) are given in Appendix C.

3.2. *Boundary Terms in Transport Equation*

The boundary flux contributions to the transport operator in equation (3.11) are evaluated as follows. Given a ray $\hat{\boldsymbol{\Omega}}$, we compute for each segment of the boundary of each zone the scalar product $\hat{\boldsymbol{\Omega}} \cdot \hat{\boldsymbol{n}}$. For example, for the mth segment of the zone, we have

$$(\hat{\boldsymbol{\Omega}} \cdot \hat{\boldsymbol{n}})_m = \cos\theta\, \hat{\boldsymbol{n}}_m^z + \sin\theta\cos\psi\, \hat{\boldsymbol{n}}_m^r . \tag{3.15}$$

For the given ray denote by $\tilde{I}$ the intensity on the upwind side of a zone boundary segment:

$$\tilde{I}_k = \begin{cases} I_k & \text{on } \partial^+ V , \\ I_k^* & \text{on } \partial^- V . \end{cases} \tag{3.16}$$

The total spatial transport contribution to equation (3.11) can then be written as

$$D_l = -\cos\theta (I\,\partial_z w_l) - \sin\theta\cos\psi (I\,\partial_r w_l) + \sum_{m=1}^{4} \int dA_m\, w_l \tilde{I}(\hat{\boldsymbol{\Omega}} \cdot \hat{\boldsymbol{n}})_m , \tag{3.17}$$

where the sum is over the four boundary segments comprising ∂V. If we define the expressions

$$(\hat{\boldsymbol{\Omega}} \cdot \hat{\boldsymbol{n}})_m^+ \equiv \tfrac{1}{2}[(\hat{\boldsymbol{\Omega}} \cdot \hat{\boldsymbol{n}})_m + |(\hat{\boldsymbol{\Omega}} \cdot \hat{\boldsymbol{n}})_m|] \quad \text{and} \quad (\hat{\boldsymbol{\Omega}} \cdot \hat{\boldsymbol{n}})_m^- \equiv \tfrac{1}{2}[(\hat{\boldsymbol{\Omega}} \cdot \hat{\boldsymbol{n}})_m - |(\hat{\boldsymbol{\Omega}} \cdot \hat{\boldsymbol{n}})_m|] ,$$

then we can express equation (3.17) as

$$D_l = -\cos\theta(I\,\partial_z w_l) - \sin\theta\cos\psi(I\,\partial_r w_l) + \sum_{m=1}^{4} \int dA_m\, w_l[I(\hat{\boldsymbol{\Omega}} \cdot \hat{\boldsymbol{n}})_m^+ + I^*(\hat{\boldsymbol{\Omega}} \cdot \hat{\boldsymbol{n}})_m^-] , \tag{3.18}$$

$l = 1, 2, 3, 4$. Performing the boundary integrations, the D_l have the explicit forms

$$\begin{aligned} D_1 = {} & -\cos\theta(I\,\partial_z w_1) - \sin\theta\cos\psi(I\,\partial_r w_1) + \frac{\pi}{6}(\hat{\boldsymbol{\Omega}} \cdot \hat{\boldsymbol{n}})_1^+ \Delta S_1[I_1(3r_1 + r_2) + I_2(r_1 + r_2)] \\ & + \frac{\pi}{6}(\hat{\boldsymbol{\Omega}} \cdot \hat{\boldsymbol{n}})_1^- \Delta S_1[I_5(3r_1 + r_2) + I_6(r_1 + r_2)] + \frac{\pi}{6}(\hat{\boldsymbol{\Omega}} \cdot \hat{\boldsymbol{n}})_4^+ \Delta S_4[I_1(3r_1 + r_4) + I_4(r_1 + r_4)] \\ & + \frac{\pi}{6}(\hat{\boldsymbol{\Omega}} \cdot \hat{\boldsymbol{n}})_4^- \Delta S_4[I_{12}(3r_1 + r_4) + I_{11}(r_1 + r_4)] , \end{aligned} \tag{3.19}$$

$$\begin{aligned} D_2 = {} & -\cos\theta(I\,\partial_z w_2) - \sin\theta\cos\psi(I\,\partial_r w_2) + \frac{\pi}{6}(\hat{\boldsymbol{\Omega}} \cdot \hat{\boldsymbol{n}})_2^+ \Delta S_2[I_2(3r_2 + r_3) + I_3(r_2 + r_3)] \\ & + \frac{\pi}{6}(\hat{\boldsymbol{\Omega}} \cdot \hat{\boldsymbol{n}})_2^- \Delta S_2[I_7(3r_2 + r_3) + I_8(r_2 + r_3)] + \frac{\pi}{6}(\hat{\boldsymbol{\Omega}} \cdot \hat{\boldsymbol{n}})_1^+ \Delta S_1[I_2(3r_2 + r_1) + I_1(r_2 + r_1)] \\ & + \frac{\pi}{6}(\hat{\boldsymbol{\Omega}} \cdot \hat{\boldsymbol{n}})_1^- \Delta S_1[I_6(3r_2 + r_1) + I_5(r_2 + r_1)] , \end{aligned} \tag{3.20}$$

$$\begin{aligned} D_3 = {} & -\cos\theta(I\,\partial_z w_3) - \sin\theta\cos\psi(I\,\partial_r w_3) + \frac{\pi}{6}(\hat{\boldsymbol{\Omega}} \cdot \hat{\boldsymbol{n}})_3^+ \Delta S_3[I_3(3r_3 + r_4) + I_4(r_3 + r_4)] \\ & + \frac{\pi}{6}(\hat{\boldsymbol{\Omega}} \cdot \hat{\boldsymbol{n}})_3^- \Delta S_3[I_9(3r_3 + r_4) + I_{10}(r_3 + r_4)] + \frac{\pi}{6}(\hat{\boldsymbol{\Omega}} \cdot \hat{\boldsymbol{n}})_2^+ \Delta S_2[I_3(3r_3 + r_2) + I_2(r_3 + r_2)] \\ & + \frac{\pi}{6}(\hat{\boldsymbol{\Omega}} \cdot \hat{\boldsymbol{n}})_2^- \Delta S_2[I_8(3r_3 + r_2) + I_7(r_3 + r_2)] , \end{aligned} \tag{3.21}$$

and

$$\begin{aligned} D_4 = {} & -\cos\theta(I\,\partial_z w_4) - \sin\theta\cos\psi(I\,\partial_r w_4) + \frac{\pi}{6}(\hat{\boldsymbol{\Omega}} \cdot \hat{\boldsymbol{n}})_4^+ \Delta S_4[I_4(3r_4 + r_1) + I_1(r_4 + r_1)] \\ & + \frac{\pi}{6}(\hat{\boldsymbol{\Omega}} \cdot \hat{\boldsymbol{n}})_4^- \Delta S_4[I_{11}(3r_4 + r_1) + I_{12}(r_4 + r_1)] + \frac{\pi}{6}(\hat{\boldsymbol{\Omega}} \cdot \hat{\boldsymbol{n}})_3^+ \Delta S_3[I_4(3r_4 + r_3) + I_3(r_4 + r_3)] \\ & + \frac{\pi}{6}(\hat{\boldsymbol{\Omega}} \cdot \hat{\boldsymbol{n}})_3^- \Delta S_3[I_{10}(3r_4 + r_3) + I_9(r_4 + r_3)] , \end{aligned} \tag{3.22}$$

where ΔS_l is the length of boundary segment l. We note that half of the coefficients of the boundary terms are actually equal to zero for a given ray. Those that do not vanish are either coefficients of the interior intensities I_l, $l = 1, 2, 3, 4$, in which case they contribute to the transport matrix, or they multiply external intensities that are upwind of the zone and have been obtained earlier in the sweep.

3.3. *Angle Binning and Angle Transport Differencing*

The angular structure of the intensity is such that the approximate solution is taken to be constant within each solid angle bin. The azimuthal angle transport term appearing in equation (3.11) is treated in an explicit upwind fashion. The bins are divided into sets, each set characterized by a mean polar angle θ_i. Within a set, the rays are calculated in descending order of azimuthal angle, starting with the ray nearest the direction $\psi = \pi$ toward the z-axis, since azimuthal angle decreases monotonically along the hyperbolic characteristics of equation (2.4). In this way information that flows along characteristics in the analytic equation is passed through a sequence of tangent fields in the numerical approximation. If $\Delta\psi_{i,n}$ is the azimuthal angular width of the nth ray in the ith polar angle strip, the term

$$\frac{\partial}{\partial\psi}\left[\sin\psi\left(\frac{Iw_l}{r}\right)\right. \tag{3.23}$$

is represented by the discretized form

$$\frac{1}{\Delta\Psi_{i,n}}\left\{\sin\psi_{i,n}\left[\frac{I(i,\,n-1)w_l}{r}\right]-\sin\psi_{i,n+1}\left[\frac{I(i,\,n)w_l}{r}\right]\right\}, \tag{3.24}$$

where $\psi_{i1}=\pi$ and the pair (i, n) denotes the solid-angle bin. The form (3.24) preserves the conservative property of expression (3.23); radiation that leaves one $\Delta\psi$ bin appears in the next bin. As the simplest possible upwind donor cell advection scheme, it is, in fact, an example of the DFE method wherein the space of allowed functions of ψ is restricted to a constant. The idea of using higher order elements to describe the angular structure in the context of the discrete ordinates approximation has been pursued by Mordant, who tested a linear form on a space-angle phase space. We have, ourselves, experimented with an element that is the product of a bilinear form on spatial quadrilaterals and a linear form in azimuthal angle. A problem with such constructions is that they can be inherently incompatible with the idea of ordering the zones in an unambiguous way from upwind to downwind. Thus, if a single mean direction is associated with a ray, then it is possible to determine for a given spatial interface that one side is downwind of the other. All of the radiation in the solid-angle element moves in the mean direction from the upwind to the downwind side. With a higher order angular structure, one can have "interface straddling"; the sense of the upwind-downwind relation between adjacent zones changes from one part of the solid-angle element to another. It is then impossible to solve the zones sequentially without sacrificing a certain degree of positivity, unless one is willing to restore the lower order approximation to the spatial transport part of equation (3.11). "Interface straddling" need not be a problem, of course, if the spatial grid is sufficiently regular. A grid of rectangular zones, for example, can be oriented so that "interface straddling" does not occur. For general Lagrangian meshes, however, the problem is intrinsic. For this reason we have used the low-order approximation and the simple differencing scheme given by expression (3.24).

The discretized version of the radiation transport equation (2.4) implemented in ALTAIR is obtained upon substitution of expressions (3.18) and (3.24) in equation (3.11):

$$\left(\frac{1}{c\Delta t}+\chi\right)V_l I_l(i,\,n)+D_l(i,\,n)+\sin\theta_i\frac{\sin\psi_{i,n+1}}{\Delta\psi_{i,n}}\left[\frac{I(i,\,n)w_l}{r}\right]=\eta_l V_l+\frac{1}{c\Delta t}V_l I_l^0(i,\,n)+\sin\theta_i\frac{\sin\psi_{i,n}}{\Delta\psi_{i,n}}\left[\frac{I(i,\,n-1)w_l}{r}\right], \tag{3.25}$$

$l=1, 2, 3, 4$, where the implicit time differencing is shown.

4. NUMERICAL DISCRETIZATION OF THE COMBINED TENSOR MOMENT EQUATION

4.1. *Triangulated Quadrilateral Mesh*

The combined tensor moment equation (2.31) and the underlying transport equation (2.4) are taken to have in common a solution domain R with convex boundary ∂R. The numerical grid that we use to define material properties on R is a logically rectangular mesh of convex quadrilateral zones. Quantities such as population densities, electron density and temperature, and opacities are considered to be constant over a quadrilateral zone. To define the radiation degrees of freedom, we subdivide each quadrilateral element into four triangles, as shown in Figure 1. The mean intensity is then defined at the nodes of the original quadrilateral mesh, which we shall call a-nodes, and at the c-nodes defined by the triangles within each quad. In this way, we attempt to take account of the fact that, depending on the source configuration, the physical energy density may exhibit an extremum within a zone as well as at a corner node.

We construct discrete representations of the moment equation and the transport equation by assuming that the approximate numerical solutions of these equations are restricted to a particular function space within each zone. In the case of the moment equation, these finite elements are taken to be triangular and linear. That is, the mean intensity J_ν is considered to vary linearly over each of the four triangles within a quadrilateral zone. We also take the representation to be continuous, i.e., J_ν is single-valued at each node. It is convenient to represent J_ν on a triangle as an expansion in terms of a particular set of basis functions. Referring to the typical triangle in Figure 2, its cross-section area is

$$A_{012}=\tfrac{1}{2}[r_1(z_0-z_2)+r_2(z_1-z_0)+r_0(z_2-z_1)]\,. \tag{4.1}$$

The triangle volume of revolution around the z-axis is then

$$V_{012}=2\pi\int_\Delta r\,dr\,dz=2\pi\bar{r}_{012}A_{012}\,, \tag{4.2}$$

where

$$\bar{r}_{012}=\tfrac{1}{3}(r_0+r_1+r_2)\,. \tag{4.3}$$

The linear basis functions are taken to be

$$w_0(r,\,z)=\frac{1}{2A_{012}}[r_1(z-z_2)+r_2(z_1-z)+r(z_2-z_1)]\,, \tag{4.4a}$$

$$w_1(r,\,z)=\frac{1}{2A_{012}}[r(z_0-z_2)+r_2(z-z_0)+r_0(z_2-z)]\,, \tag{4.4b}$$

and

$$w_2(r,\,z)=\frac{1}{2A_{012}}[r_1(z_0-z)+r(z_1-z_0)+r_0(z-z_1)]\,. \tag{4.4c}$$

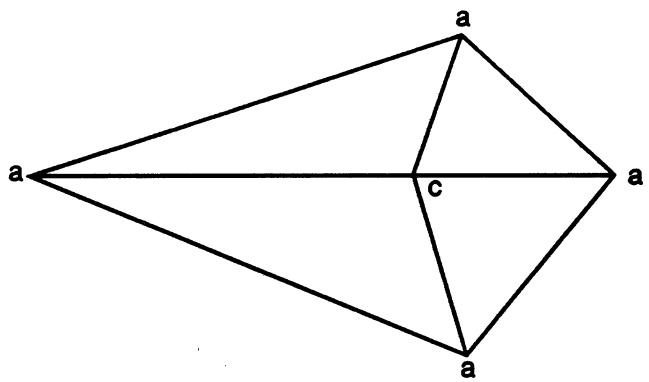

FIG. 1

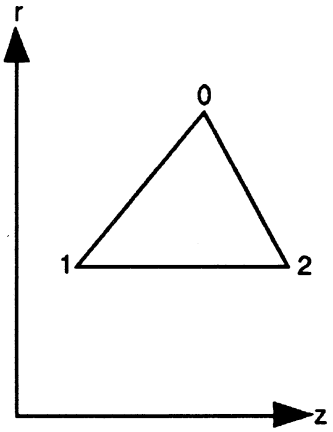

FIG. 2

FIG. 1.—Quadrilateral mesh element has *a*-nodes at its corners and a *c*-node at its centroid.
FIG. 2.—Node points of a typical triangle and orientation of *r*-*z* coordinate system.

We have

$$w_n(r_m, z_m) = \delta_{nm}\,, \qquad n, m = 0, 1, 2\,, \tag{4.5}$$

and the completeness relation

$$\sum_{n=0}^{2} w_n(r, z) = 1 \tag{4.6}$$

for points (r, z) within the triangle. The w_n basis functions are also used to associate with each node a fraction of the volume of the triangle:

$$V_n = 2\pi \int_\Delta r\,dr\,dz\,w_n(r, z) = \left(\frac{1}{4} + \frac{1}{12}\frac{r_n}{\bar{r}_{012}}\right)V_{012} = \frac{\pi}{2}\left(\bar{r}_{012} + \frac{1}{3}r_n\right)A_{012}\,, \qquad n = 0, 1, 2\,. \tag{4.7}$$

The partial volumes sum to the volume of the triangle:

$$V_{012} = \sum_{n=0}^{2} v_n\,. \tag{4.8}$$

The mean intensity is represented as

$$J(r, z) = \sum_{n=0}^{2} J_n\,w_n(r, z)\,, \tag{4.9}$$

where the J_n are the nodal values; the frequency subscript has been omitted for clarity.

4.2. *Projections of the Flux Divergence*

If there are N nodes, then we need N linearly independent equations for the mean intensity. Rather than try to difference directly the combined tensor moment equation (2.31), we follow a two-step procedure. The first step is to discretize the zeroth-moment equation (2.17). This is done by picking a functional form for the Eddington flux $\boldsymbol{H}$, performing the indicated differential operations, multiplying equation (2.17) by a particular test function associated with a node, and then integrating over the support of the test function. The second step is to substitute in the resulting discretized zeroth-moment equation the expressions for $\boldsymbol{H}$ in terms of J and $\boldsymbol{T}$ implied by the first-moment equations (2.22) and (2.23) and the assumed functional form of $\boldsymbol{H}$.

The choice we make for the functional form of $\boldsymbol{H}$ is that it be constant over a triangle. The values of the components H_r and H_z are then obtained by applying a volume-averaging operator to equations (2.29) and (2.30). To proceed with the discretization of the zeroth-moment equation, we represent it in the form

$$\frac{1}{c}\frac{\partial J}{\partial t} + \nabla \cdot \boldsymbol{H} = \eta - \chi J\,; \tag{4.10}$$

cf. equation (2.24), where η is the total emissivity and χ the total opacity. The test functions we use to generate a representation of equation (4.10) at a particular node are of the hat, or pyramid, type; they have the value unity at the node under consideration and vary linearly over each adjoining triangle to zero at the adjacent nodes. The test function W is thus identical, within a certain triangle, to the basis function (4.4) on that triangle that has value unity at that node. By applying these hat functions to *a*- and *c*-nodes, we generate the two types of connectivity shown in Figure 3.

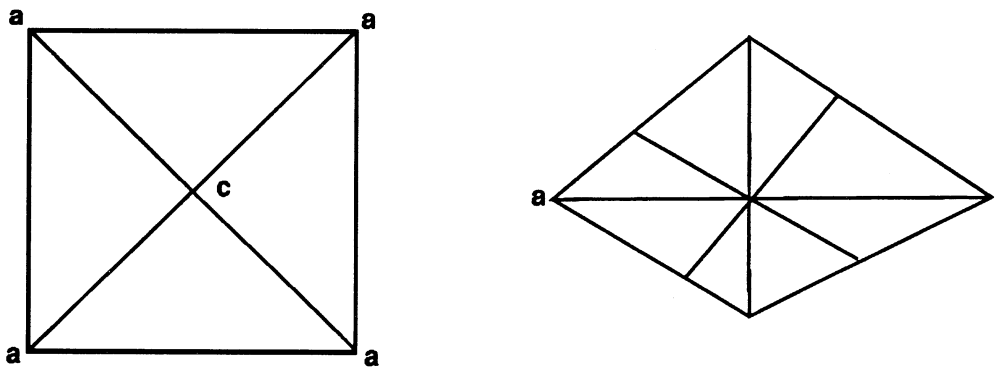

FIG. 3.—Five point c-node and a-node stencils.

We substitute the expressions for J, $\boldsymbol{H}$, χ, and η in equation (4.10) and perform the differentiations. Since $\boldsymbol{H}$ is constant on each triangle, it is discontinuous across triangle interfaces. When the divergence is taken, we thus obtain regular contributions from triangle interiors plus delta-function singularities at these interfaces, where the strength of the singularity is given by the normal component of the flux discontinuity. The operation of multiplying by a reference node hat function and integrating over its support then generates from $\nabla \cdot \boldsymbol{H}$ an expression that can be written as a sum over adjoining triangles:

$$\nabla \cdot \boldsymbol{H} \rightarrow \sum_{l=1}^{L} \left[\int_{\Delta_l} dV\, W \nabla \cdot \boldsymbol{H}_l + \tfrac{1}{2} \int_{\partial \Delta_l} dA\, W \hat{\boldsymbol{n}} \cdot [\mathbf{H}] \right], \tag{4.11}$$

where

$$[\boldsymbol{H}] = \boldsymbol{H}(\text{exterior}) - \boldsymbol{H}_l\,, \tag{4.12}$$

and L is 4 or 8, depending on whether this is a c-node or an a-node (see Fig. 3). The volume integration indicated in equation (4.11) is over the volume of rotation about the z-axis (the symmetry axis) of the lth triangle. The surface integral is over the boundary of that triangle, where $\hat{\boldsymbol{n}}$ is the unit outwardly directed normal on $\partial \Delta_l$. The factor of $\frac{1}{2}$ appearing in this term comes from associating half the singular interface term with each triangle. In equation (4.12), $\boldsymbol{H}_l$ is the flux on the lth triangle, and $\boldsymbol{H}$ (exterior) is the neighboring flux; in general, it is a different constant on each of the three segments of $\partial \Delta_l$. We now reformulate the expression in equation (4.11) by integrating each of the volume integrals by parts:

$$\sum_{l=1}^{L} \left\{ \int_{\Delta l} dV\, W \nabla \cdot \boldsymbol{H}_l + \tfrac{1}{2} \int_{\partial \Delta_l} dA\, W \hat{\boldsymbol{n}} \cdot [\boldsymbol{H}(\text{exterior}) - \boldsymbol{H}_l] \right\} = \sum_{l=1}^{L} \left\{ - \int_{\Delta_l} dV\, \boldsymbol{H}_l \cdot \nabla W + \tfrac{1}{2} \int_{\partial \Delta_l} dA\, W \hat{\boldsymbol{n}} \cdot [\boldsymbol{H}(\text{exterior}) + \boldsymbol{H}_l] \right\}. \tag{4.13}$$

One notes that the surface integral over the segment of $\partial \Delta_l$ opposite the reference node vanishes because $W = 0$ on that segment. Furthermore, for those segments touching the reference node, as long as there is actually a triangle on each side of the segment, the two surface integrals over the segment due to the triangles on either side cancel as a result of the opposite orientations of $\hat{\boldsymbol{n}}$. Thus, if the reference node is an interior node, as shown in Figures 4*a* and 4*b*, the surface contribution to equation (4.13) vanishes completely. If it is a boundary node, as shown in Figure 4c, we pick up the uncanceled surface terms along ∂R, where $W \neq 0$. Thus,

$$\nabla \cdot \boldsymbol{H} \rightarrow \sum_{l=1}^{L} \left\{ - \int_{\Delta_l} dV\, \boldsymbol{H}_l \cdot \nabla W + \tfrac{1}{2} \int_{\partial R} dA\, W \hat{\boldsymbol{n}} \cdot [\boldsymbol{H}(\text{exterior}) + \boldsymbol{H}_l] \right\}. \tag{4.14}$$

The sum over volume integrals in equation (4.14) is expressed in terms of cylindrical coordinates as

$$\nabla \cdot \boldsymbol{H} \rightarrow -2\pi \sum_{l=1}^{L} \left(H_{rl} \int_{\Delta l} \frac{\partial W}{\partial r}\, r\, dr\, dz + H_{zl} \int_{\Delta l} \frac{\partial W}{\partial z}\, r\, dr\, dz \right), \tag{4.15}$$

where the constant flux components have been taken outside the integrals. Let triangle 012 of Figure 2 by a typical triangle in the sum, and let node zero be the reference node. Then $W = w_0$ on 012, where w_0 is the basis function given by equation (4.4a). We have

$$\frac{\partial w_0}{\partial r} = \frac{1}{A_{012}} (z_2 - z_1) \quad \text{and} \quad \frac{\partial w_0}{\partial z} = \frac{1}{2A_{012}} (r_1 - r_2)\,, \tag{4.16}$$

so that

$$\int_{012} dV\, \boldsymbol{H} \cdot \nabla W = H_{r012} \frac{V_{012}}{2A_{012}} (z_2 - z_1) - H_{z012} \frac{V_{012}}{2A_{012}} (r_2 - r_1)\,. \tag{4.17}$$

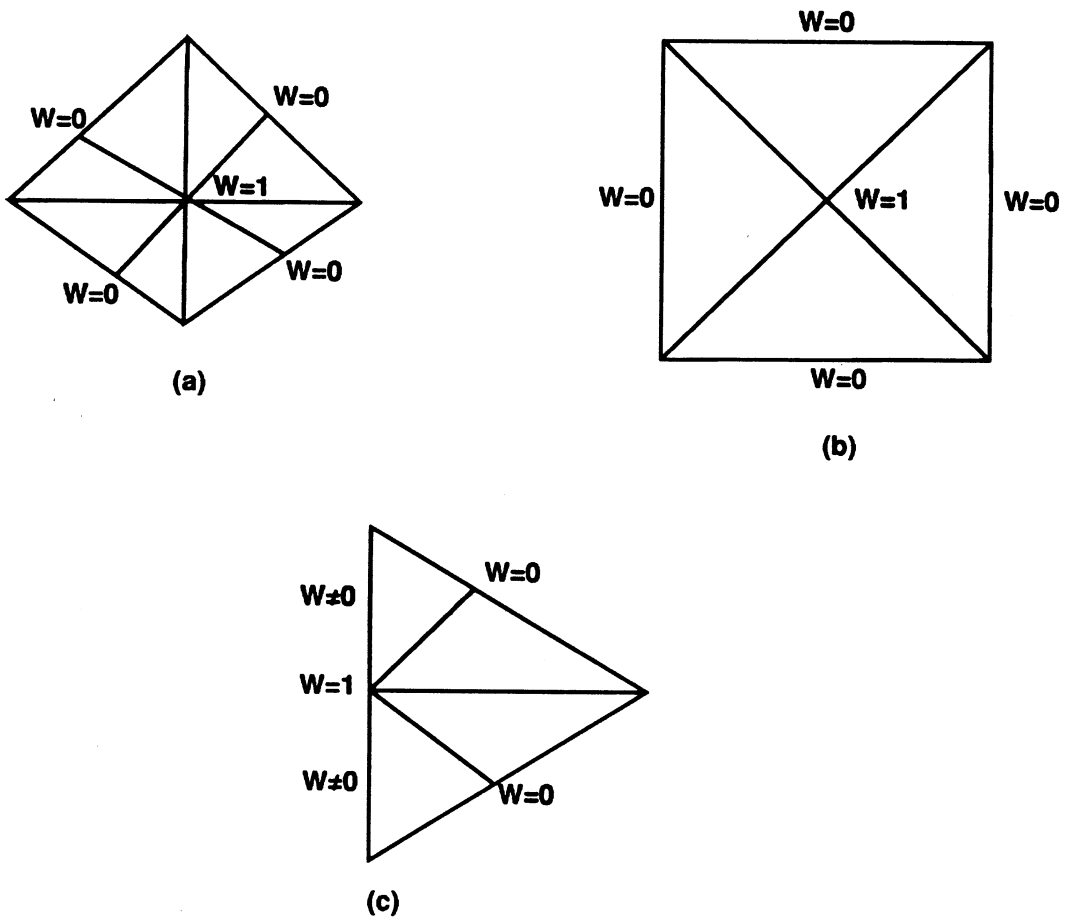

FIG. 4.—(*a*) Interior *a*-node. (*b*) Interior *c*-node. (*c*) Boundary *a*-node. There are no boundary *c*-nodes.

With an obvious change of notation,

$$-\sum_{l=1}^{L}\int_{\Delta_l} dV\, \boldsymbol{H}_l\cdot\nabla W = -\frac{1}{2}\sum_{l=1}^{L}\frac{V_l}{A_l}\left[H_{rl}(z_{l+1}-z_l) - H_{zl}(r_{l+1}-r_l)\right], \tag{4.18}$$

where, given the orientation of our coordinates, the sense of increasing l is counterclockwise about the reference node. We note that the V_l in equation (4.18) is the full triangle volume and not just that portion associated with a particular node as in equation (4.8).

In place of the boundary term

$$\tfrac{1}{2}\int_{\partial R} dA\, W\hat{\boldsymbol{n}}\cdot[\mathrm{H(exterior)} + \boldsymbol{H}_l]$$

in equation (4.14), we use a numerical evaluation of

$$\int_{\partial R} dA\, W(\beta J - \beta J^- + \boldsymbol{H}^-\cdot\hat{\boldsymbol{n}}), \tag{4.19}$$

where $\boldsymbol{H}^-$ and β have been defined in equations (2.32)–(2.34).

As shown in Figure 5, equation (4.19) can be expressed as a sum of integrals over the boundary segments S_2 and S_1 on either side of reference node zero. Although $\boldsymbol{H}$ is considered to be constant in the evaluation of the volume integral in equation (4.18), the expression in parentheses in equation (4.19) is taken to vary linearly over each segment. Using the basis functions in equation (4.4) and identifying $W = w_0$, one obtains effective-area weight functions for segment S_1:

$$A_{10} = \int_{S_1} dA\, w_0^2 = \pi\Delta S_{01}(\tfrac{1}{2}r_0 + \tfrac{1}{6}r_1), \qquad A_{11} = \int_{S_1} dA\, w_0 w_1 = \pi\Delta S_{01}(\tfrac{1}{6}r_0 + \tfrac{1}{6}r_1), \tag{4.20}$$

where ΔS_{01} is the length of S_1. Likewise, for segment S_2:

$$A_{20} = \int_{S_2} dA\, w_0^2 = \pi\Delta S_{20}(\tfrac{1}{2}r_0 + \tfrac{1}{6}r_2), \qquad A_{22} = \int_{S_2} dA\, w_0 w_2 = \pi\Delta S_{20}(\tfrac{1}{6}r_0 + \tfrac{1}{6}r_2). \tag{4.21}$$

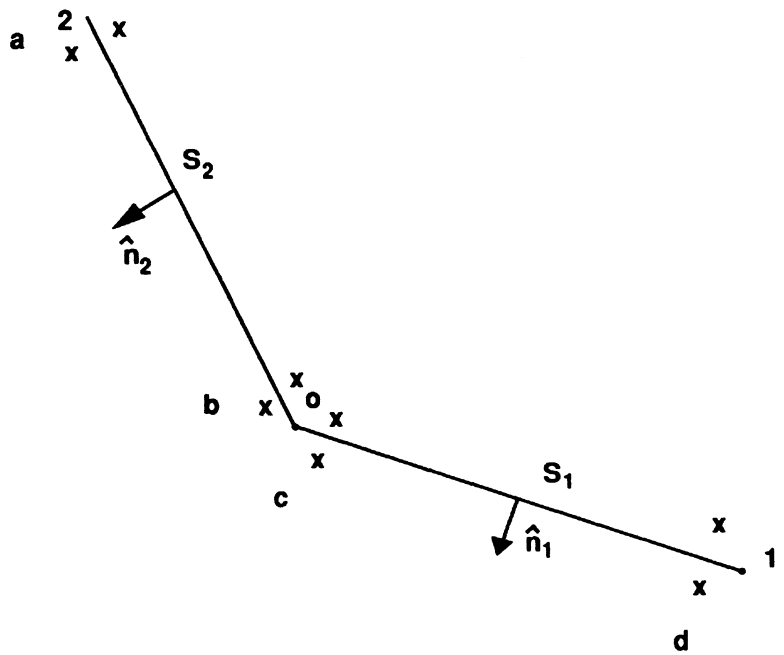

FIG. 5.—The part of the boundary ∂R centered on the boundary reference node zero consists of segments S_2, between nodes 2 and 0, and S_1 between nodes 0 and 1. The crosses mark the location of specifc intensity degrees of freedom. They occur pairwise on ∂R. Pairs are labeled *a*, *b*, *c* and *d*.

Anticipating the discussion below of the transport equation, the intensity is considered to be multivalued at *a*-nodes. Along ∂R these degrees of freedom are arranged pairwise, as shown in Figure 5. As a result, the values of β and $\boldsymbol{H}^- \cdot \hat{\boldsymbol{n}}$ associated with pair *b* in Figure 5 are not necessarily equal to the values associated with pair *c*. The evaluation of expression (4.19) takes account of this fact:

$$\int_{\partial R} dA\, W(\beta J - \beta J^- + \boldsymbol{H}^- \cdot \hat{\boldsymbol{n}}) = A_{10}[\beta_c J_0 - (\beta J^-)_c + (\boldsymbol{H}^- \cdot \hat{\boldsymbol{n}})_c] + A_{11}[\beta_d J_1 - (\beta J^-)_d + (\boldsymbol{H}^- \cdot \hat{\boldsymbol{n}})_d]$$
$$+ A_{20}[\beta_b J_0 - (\beta J^-)_b + (\boldsymbol{H}^- \cdot \hat{\boldsymbol{n}})_b] + A_{22}[\beta_a J_2 - (\beta J^-)_a + (\boldsymbol{H}^- \cdot \hat{\boldsymbol{n}})_a] \,. \quad (4.22)$$

One observes that J_0 is coupled to J_1 and J_2 through the boundary condition. Equation (4.22) is added to equation (4.18) to complete the discretization of $\nabla \cdot \boldsymbol{H}$.

4.3. *Projections of Source and Sink Terms*

We next apply the operations of reference node hat function multiplication and volume integration to the emission, absorption, and time evolution terms in the zeroth-moment equation (4.10). The result can again be expressed as a sum over all triangles that have the reference node as a vertex:

$$\int dV\, W\left(\frac{1}{c}\frac{\partial J}{\partial t} + \chi J - \eta\right) = \sum_{l=1}^{L} \int_{\Delta l} dV\, W\left(\frac{1}{c}\frac{\partial J}{\partial t} + \chi J - \eta\right) . \quad (4.23)$$

Let triangle 012 of Figure 2 be a typical triangle in the sum, and let node zero be the reference node. Then $W = w_0$ on 012, where w_0 is given by equation (4.4a). The mean intensity J is linear on the triangle and is represented by the expansion in equation (4.7) in terms of its nodal values. The opacity χ is constant, so the product χJ is linear also. Finally, the emissivity η is linear, since it contains quantities that either are constant over the zone or are linear (see eq. [2.28]). Thus the evaluation of equation (4.23) consists of calculating

$$\sum_{n=0}^{2} \left[\frac{1}{c}\frac{\partial J_n}{\partial t} + (\chi J)_n - \eta_n\right] \int_{012} dV\, w_0\, w_n \quad (4.24)$$

for each triangle in the sum.

A distinctive feature of equation (4.24) is that the representation of the processes of time evolution, absorption, and scattering at a particular node is not local to that node; that is, equation (4.24) involves not just J_0, but J_1 and J_2 as well. A local representation can easily be obtained by the ad hoc modification

$$\int_{012} dV\, w_0\, w_n \to \delta_{0n} \int_{012} dV\, w_0 \,, \quad (4.25)$$

so that expansion (4.24) becomes

$$\left[\frac{1}{c}\frac{\partial J_0}{\partial t} + (\chi J)_0 - \eta_0\right] V_0 , \tag{4.26}$$

where

$$V_0 = \int_{012} dV\, w_0$$

is the fraction of the triangle volume associated with node zero given by equation (4.8). The effect of this modification, sometimes called mass lumping, is to diagonalize, with respect to time evolution, absorption, and scattering, the spatial matrix that must be inverted to obtain the mean intensity. Because of the completeness property in equation (4.6) satisfied by the basis functions, the full triangle volume is represented in the global system matrix in both formulations. However, the two schemes are not equivalent; they do not give the same answers. We have found that the use of expression (4.26) greatly reduces the frequency of occurrence of negative values of the mean intensity, relative to expression (4.24). It also tends to eliminate Gibbs oscillations, that is, the tendency of the numerical solution to ring in the vicinity of sharp variations in the source function. A third benefit that accrues to the use of equation (4.26) is that the double-splitting iteration technique, described in Paper I, is simplified. Our review of this procedure in Paper I anticipates the replacement of the canonical formulation (4.24) by expression (4.26).

4.4. *Complete Zeroth-Moment Equation in Difference Form*

Expression (4.26) is substituted in the summation of equation (4.23). One obtains

$$\int dV\, W\left(\frac{1}{c}\frac{\partial J}{\partial t} + \chi J - \eta\right) = \frac{1}{c}\frac{\partial J_0}{\partial t}\sum_{l=1}^{L} V_{0l} + J_0 \sum_{l=1}^{L} V_{0l}\chi_l - \sum_{l=1}^{L} V_{0l}\eta_l , \tag{4.27}$$

where V_{0l} is the part of the volume of the lth triangle associated with reference node zero, as in equation (4.8). To this are added equations (4.18) and (4.22) to complete the discretization of the zeroth-moment equation:

$$\begin{aligned}
&\frac{1}{2}\frac{\partial J_0}{\partial t}\sum_{l=1}^{L} V_{0l} + J_0 \sum_{l=1}^{L} V_{0l}\chi_l - \sum_{l=1}^{L} V_{0l}\eta_l - \frac{1}{2}\sum_{l=1}^{L}\frac{V_l}{A_l}\left[H_{rl}(z_l + 1 - z_l) - H_{zl}(r_l + 1 - r_l)\right] \\
&\quad + A_{10}[\beta_c J_0 - (\beta J^-)_c + (\boldsymbol{H}^- \cdot \hat{\boldsymbol{n}})_c] + A_{11}[\beta_d J_1 - (\beta J^-)_d + (\boldsymbol{H}^- \cdot \hat{\boldsymbol{n}})_d] \\
&\quad + A_{20}[\beta_b J_0 - (\beta J^-)_b + (\boldsymbol{H}^- \cdot \hat{\boldsymbol{n}})_b] + A_{22}[\beta_a J_2 - (\beta J^-)_a + (\boldsymbol{H}^- \cdot \hat{\boldsymbol{n}})_a] = 0 .
\end{aligned} \tag{4.28}$$

4.5. *Conservation*

The second step of the two-step procedure leading to the discretization of the combined tensor moment equation (2.31) is to construct from equations (2.29) and (2.30) expressions for the Eddington flux components H^r and H^z. It has been assumed in the development of equation (4.28) that these fluxes are constant on a triangle, but the scheme for generating the values themselves remains to be specified. It should be noted that the conservative nature of equation (4.28), and therefore the conservative nature of the combined tensor moment equation with respect to volume integration over R, is independent of the means used to determine $\boldsymbol{H}$. Thus, the volume integral of the zeroth-moment equation over spatial domain R is represented by summing equation (4.28) over all nodes. A given triangle will contribute 3 times to this sum. For the triangle in Figure 2, the total contribution to the flux divergence is

$$\frac{V}{A} H_r[(z_2 - z_1) + (z_0 - z_2) + (z_1 - z_0)] - \frac{V}{A} H_z[(r_2 - r_1) + (r_0 - r_2) + (r_1 - r_0)] = 0 , \tag{4.29}$$

independent of the values of H_r and H_z, where V and A are the volume and area of the triangle. Hence the quantity

$$\sum_{n=1}^{N} J_n \sum_{l=1}^{L(n)} V_{nl} \tag{4.30}$$

is conserved in time, modulo sources, sinks, and ∂R boundary flux terms. The sum over n in equation (4.30) is over the N nodes in the solution domain R, while the sum on l is over the triangles associated with each node. $L(n)$ is, as before, either 4 or 8, depending on whether node n is a c- or an a-node, and V_{nl} is the part of the volume of the lth triangle associated with the nth node, given by an expression like that in equation (4.8).

4.6. *Zone-Average Flux from First-Moment Equation*

Upon substituting in equations (2.29) and (2.30) the expansion in equation (4.7) for J on a triangle, and a corresponding linear expression for the product $\boldsymbol{TJ}$ (representing the radiation pressure), one obtains forms for H_r and H_z on the triangle that are linear in z and rational in r. These expressions are reduced to the single numbers (per frequency) used in equation (4.28) by volume averaging. Since the differentiations prescribed in equations (2.29) and (2.30) are performed analytically, as contrasted with numerical differentiations, the operation of differentiating a product of functions is represented exactly. This means that the volume averages of equations (2.29) and (2.30) can be constructed with the few simple terms developed in Appendix A.

The flux components now follow from equations (2.29) and (2.30), the volume averages of which we write using the time superscript convention of equation (2.26):

$$(H_r)_{012} = \zeta\left[\frac{1}{c\Delta t} H_r^0 - \frac{1}{r}\frac{\partial}{\partial r}(rT_{rr}J) - \frac{\partial}{\partial z}(T_{rz}J) + \frac{1}{r}(1 - T_{rr} - T_{zz})J\right]_{012}, \tag{4.31a}$$

$$(H_z)_{012} = \zeta\left[\frac{1}{c\Delta t} H_z^0 - \frac{1}{r}\frac{\partial}{\partial r}(rT_{rz}J) - \frac{\partial}{\partial z}(T_{zz}J)\right]_{012}, \tag{4.31b}$$

where, given its definition following equation (2.28), the constant ζ has been taken outside the volume-averaging operator. Using equations (A4) and (A6) we find

$$\left[\frac{1}{r}\frac{\partial}{\partial r}(rT_{rr}J)\right]_{012} = \left[\frac{\partial}{\partial r}(T_{rr}J) + \frac{T_{rr}J}{r}\right]_{012}$$

$$= \frac{1}{2A_{012}}[T_{rr0}J_0(z_2 - z_1) + T_{rr1}J_1(z_0 - z_2) + T_{rr2}J_2(z_1 - z_0)] + \frac{T_{rr0}J_0 + T_{rr1}J_1 + T_{rr2}J_2}{r_0 + r_1 + r_2}, \tag{4.32}$$

$$\left[\frac{\partial}{\partial z}(T_{rz}J)\right]_{012} = -\frac{1}{2A_{012}}[T_{rz0}J_0(r_2 - r_1) + T_{rz1}J_1(r_0 - r_2) + T_{rz2}J_2(r_1 - r_0)], \tag{4.33}$$

$$\left[\frac{1}{r}(1 - T_{rr} - T_{zz})J\right]_{012} = \frac{(1 - T_{rr} - T_{zz})_0 J_0 + (1 - T_{rr} - T_{zz})_1 J_1 + (1 - T_{rr} - T_{zz})_2 J_2}{r_0 + r_1 + r_2}, \tag{4.34}$$

$$\left[\frac{1}{r}\frac{\partial}{\partial r}(rT_{rz}J)\right]_{012} = \left[\frac{\partial}{\partial r}(T_{rz}J) + \frac{T_{rz}J}{r}\right]_{012}$$

$$= \frac{1}{2A_{012}}[T_{rz0}J_0(z_2 - z_1) + T_{rz1}J_1(z_0 - z_2) + T_{rz2}J_2(z_1 - z_0)] + \frac{T_{rz0}J_0 + T_{rz1}J_1 + T_{rz2}J_2}{r_0 + r_1 + r_2}, \tag{4.35}$$

and

$$\left[\frac{\partial}{\partial z}(T_{zz}J)\right]_{012} = -\frac{1}{2A_{012}}[T_{zz0}J_0(r_2 - r_1) + T_{zz1}J_1(r_0 - r_2) + T_{zz2}J_2(r_1 - r_0)]. \tag{4.36}$$

Substituting equations (4.32)–(4.36) in equation (4.31) and grouping the terms as coefficients of the J_n, one obtains

$$(H_r)_{012} = \frac{\zeta}{c\Delta t}(H_r^0)_{012} + \zeta J_0\left\{\frac{1}{2A_{012}}[T_{rz0}(r_2 - r_1) - T_{rr0}(z_2 - z_1)] + \frac{1 - 2T_{rr0} - T_{zz0}}{r_0 + r_1 + r_2}\right\}$$
$$+ \zeta J_1\left\{\frac{1}{2A_{012}}[T_{rz1}(r_0 - r_2) - T_{rr1}(z_0 - z_2)] + \frac{1 - 2T_{rr1} - T_{zz1}}{r_0 + r_1 + r_2}\right\}$$
$$+ \zeta J_2\left\{\frac{1}{2A_{012}}[T_{rz2}(r_1 - r_0) - T_{rr2}(z_1 - z_0)] + \frac{1 - 2T_{rr2} - T_{zz2}}{r_0 + r_1 + r_2}\right\} \tag{4.37}$$

and

$$(H_z)_{012} = \frac{\zeta}{c\Delta t}(H_z^0)_{012} + \zeta J_0\left\{\frac{1}{2A_{012}}[T_{zz0}(r_2 - r_1) - T_{rz0}(z_2 - z_1)] - \frac{T_{rz0}}{r_0 + r_1 + r_2}\right\}$$
$$+ \zeta J_1\left\{\frac{1}{2A_{012}}[T_{zz1}(r_0 - r_2) - T_{rz1}(z_0 - z_2)] - \frac{T_{rz1}}{r_0 + r_1 + r_2}\right\}$$
$$+ \zeta J_2\left\{\frac{1}{2A_{012}}[T_{zz2}(r_1 - r_0) - T_{rz2}(z_1 - z_0)] - \frac{T_{rz2}}{r_0 + r_1 + r_2}\right\}. \tag{4.38}$$

One should note that equations (4.37) and (4.38) are by no means the only expressions that can be generated for the Eddington flux values for substitution in the discretized zeroth-moment equation (4.28). First, the expressions need not be volume averages; they could be the values of H_r and H_z at some particular point within the triangle. Another plausible variation from equations (4.37) and (4.38) comes from assuming a differential functional form for the Eddington tensor T. The above expressions follow directly from the assumption that the product TJ, i.e., the radiation pressure, varies linearly across the triangle like J itself. This is a reasonable assumption when one considers that both moments J and K can, in principle, be constructed by angle quadratures from the specific intensity, as in equations (2.5) and (2.7). If the approximate specific intensity I_ν that is the solution to the discretized transport equation is, in fact, taken to be linear on triangles and continuous across triangle boundaries, then equations (4.37) and (4.38) have the virtue that the approximate zeroth and second moments of the specific intensity that are the solution to the discretized moment system are consistent with each other and with I_ν, in the sense that they are restricted to the same function

space. However, the use of the volume-averaging operator to represent the flux in the moment equations, in place of the linear form that would be obtained from the first moment of I_ν, results in an inconsistency between the discretized moment equations and the discretized transport equation; the two systems do not yield precisely the same answers at convergence. Further, as discussed below, we have found what we think are good reasons to employ a representation of I_ν that is neither linear on triangles nor continuous across zone interfaces. We therefore take the point of view that there is no fundamental reason, other than the simplicity of the resulting algorithm, why the product TJ need be linear.

An alternative simple approximation to the spatial variation on a triangle of the product TJ is that T and J each vary linearly. We have found that incorporating this assumption into the steps leading to the discretized representations of (H_r) and (H_z) does, in fact, result in a modest improvement in the combined tensor moment results as measured against the analytic solutions of spherically symmetric test problems. The generation of (H_r) and (H_z) parallels the development leading from equation (4.31) to equations (4.37) and (4.38). The results are

$$(H_r)_{012} = \frac{\zeta}{c\Delta t}(H_r^0)_{012} - \zeta D_r , \tag{4.39}$$

where

$$\begin{aligned} D_r = {} & J_0 \frac{V_0}{V_{012}} \left\{ \frac{\partial T_{rr}}{\partial r} + \frac{\partial T_{rz}}{\partial z} - \frac{4}{2r_0 + r_1 + r_2} \left[1 - \frac{1}{2}(2T_{rr0} + T_{rr1} + T_{rr2}) - \frac{1}{4}(2T_{zz0} + T_{zz1} + T_{zz2}) \right] \right\} \\ & + \frac{1}{2A_{012}} [(z_2 - z_1)(T_{rr})_{012} - (r_2 - r_1)(T_{rz})_{012}] \\ & + J_1 \frac{V_1}{V_{012}} \left\{ \frac{\partial T_{rr}}{\partial r} + \frac{\partial T_{rz}}{\partial z} - \frac{4}{r_0 + 2r_1 + r_2} \left[1 - \frac{1}{2}(T_{rr0} + 2T_{rr1} + T_{rr2}) - \frac{1}{4}(T_{zz0} + 2T_{zz1} + T_{zz2}) \right] \right\} \\ & + \frac{1}{2A_{012}} [(z_0 - z_2)(T_{rr})_{012} - (r_0 - r_2)(T_{rz})_{012}] \\ & + J_2 \frac{V_2}{V_{012}} \left\{ \frac{\partial T_{rr}}{\partial r} + \frac{\partial T_{rz}}{\partial z} - \frac{4}{r_0 + r_1 + 2r_2} \left[1 - \frac{1}{2}(T_{rr0} + T_{rr1} + 2T_{rr2}) - \frac{1}{4}(T_{zz0} + T_{zz1} + 2T_{zz2}) \right] \right\} \\ & + \frac{1}{2A_{012}} [(z_1 - z_0)(T_{rr})_{012} - (r_1 - r_0)(T_{rz})_{012}] . \end{aligned} \tag{4.40}$$

The factor V_{012} in equation (4.40) is the triangle volume. The terms V_n, $n = 0, 1, 2$, are the portions of V_{012} associated with triangle vertex n. Expressions for the partial derivatives are given by equations (A6), and the volume averages of the linear functions T_{kl} follow from equation (A1).

Likewise,

$$(H_z)_{012} = \frac{\zeta}{c\Delta t}(H_z^0)_{012} - \zeta D_z , \tag{4.41}$$

where the z-component of the pressure divergence is

$$\begin{aligned} D_z = {} & J_0 \frac{V_0}{V_{012}} \left(\frac{\partial T_{rz}}{\partial r} + \frac{\partial T_{zz}}{\partial z} + \frac{2T_{rz0} + T_{rz1} + T_{rz2}}{2r_0 + r_1 + r_2} \right) + \frac{1}{2A_{012}} [(z_2 - z_1)(T_{rz})_{012} - (r_2 - r_1)(T_{zz})_{012}] \\ & + J_1 \frac{V_1}{V_{012}} \left(\frac{\partial T_{rz}}{\partial r} + \frac{\partial T_{zz}}{\partial z} + \frac{T_{rz0} + 2T_{rz1} + T_{rz2}}{T_0 + 2r_1 + r_2} \right) + \frac{1}{2A_{012}} [(z_0 - z_2)(T_{rz})_{012} - (r_0 - r_2)(T_{zz})_{012}] \\ & + J_2 \frac{V_2}{V_{012}} \left(\frac{\partial T_{rz}}{\partial r} + \frac{\partial T_{zz}}{\partial z} + \frac{T_{rz0} + T_{rz1} + 2T_{rz2}}{r_0 + r_1 + 2r_2} \right) + \frac{1}{2A_{012}} [(z_1 - z_0)(T_{rz})_{012} - (r_1 - r_0)(T_{zz})_{012}] . \end{aligned} \tag{4.42}$$

For the calculations in this paper, the second alternative is adopted, so the discretization of the combined tensor moment equation is achieved when equations (4.39)–(4.42) sre substituted in equation (4.28).

4.7. *Solution of Tensor Moment Equations*

Given the specification of the three independent components of the spatial- and frequency-dependent Eddington tensor $T_\nu(r, z)$, sufficient boundary information about the normal component of the flux on the boundary ∂R of the solution domain (§ 2.5), and the atomic populations and temperature necessary to compute the sources and sinks, we are in a position to solve the combined moment equations for J_ν^{n+1} at the advanced time supplemented by the auxiliary equation for the scattering integral $\bar{J}$,

$$\bar{J} = \int_{\nu_{\min}}^{\nu_{\max}} d\nu \, \phi_\nu J_\nu , \tag{4.43}$$

where the limits of the integral extend over the bandwidth of the transition l–u under consideration.

The solution of the moment equations is only one iteration loop of the larger ETLA iterative framework that embodies ALTAIR, and here we summarize the steps that make up that framework, which has been described in greater detail in Papers I and II.

1. We specify the source functions for all lines and continua and solve equation (2.4) using our new DFE technique described in detail in § 3.1.
2. Using $I(r, z, \theta, \psi, \nu, t)$ thus obtained, we construct the components of the Eddington tensor from equation (2.21), as well as the necessary boundary information to provide closure for the combined moment equations.
3. We solve the coupled moment equations (2.31) and (2.32) by our new double-splitting iteration method described in detail in Paper I to obtain the mean intensity J_ν^{n+1} in each line and continuum at all spatial points in the r-z mesh. We discuss the spatial discretization of equation (2.31) in § 3.1.
4. We use the newly obtained mean intensities to update net radiative brackets and simultaneously solve the time-dependent rate equations, energy, and change conservation equations for the atomic populations, temperature, and electron density. We discuss the solution of the energy equation in a later paper. This completes an ETLA cycle.
5. We update γ_ν and ϵ_ν, and construct new line and continuum source functions, and return to step 1. The entire procedure is iterated to convergence as described in Paper II.

Our double-splitting iteration procedure, described in Paper I, is a technique that provides a rapid and robust solution to equation (2.31). The convergence of the iteration is accelerated with the ORTHOMIN method, one of the conjugate-residual acceleration techniques. (See Paper I and Hageman & Young 1981.) As previously described, the first split of our method generates a linear system the matrix of which has an asymmetric-banded structure with nine nonzero bands. (See § 3.1 of this paper.) We have used both direct and iterative techniques to solve this system. We applied ILUBCG, a biconjugate gradient method preconditioned with incomplete lower-upper (LU) decomposition (Hageman & Young 1981). The great advantage of this approach is that it uses significantly less memory than direct approaches. The disadvantage is that the convergence may be slow for problems run on spatial meshes that have zones with large aspect ratios (≥ 1000) near boundaries. Such meshes are not uncommon for line transport problems in two dimensions, which have a large dynamic range in line optical depth. For problems such as these, we have applied a machine-language–coded band matrix solver. The advantage is that this approach works equally well for near-uniform meshes or meshes that may have zones with large aspect ratios. The disadvantage is that the direct solution uses a great deal of central memory and can be time consuming for large meshes ($> 100 \times 100$). We minimize the cost by computing the LU decomposition of the matrix for each frequency in a transition only once, during the first double-splitting iteration. The decomposition, by far the most costly part of the banded solution, is then stored for subsequent iterations for that frequency. We also make extensive use of the solid-state disk (SSD) on the Cray YMP.

The second split in the double-splitting procedure is also described in Paper I. This involves local frequency scattering at each spatial node. Here we observe that using the updated value of J_ν^{n+1} in the nonlocal source term for the next spatial node enhances the convergence of the double-splitting procedure.

5. RESULTS

5.1. *Uniform Source on x-y Mesh*

We have performed a series of tests with ALTAIR to assess the convergence properties. In the first such test, we applied ALTAIR, in two-dimensional x-y geometry, to the two-level atom line formation problem and compared it with the two-dimensional approximate-operator iteration (AOI) code developed by Kunasz & Olson (1968) and Olson, Auer, & Buchler (1986). We studied both uniform and nonuniform thermal sources, while varying the parameters x_l (the line opacity), χ_c (the continuum opacity), ϵ (the collisional thermalization parameter), and the number of grid cells in the two-dimensional mesh. In these calculations, we have assumed (1) no velocity fields, (2) steady state, (3) two-level atom source function with complete redistribution in the line, (4) Doppler profile for the line. These assumption have been made for these tests only and are not limitations of ALTAIR. In this section, the uniform source will be treated; the nonuniform source will be taken up in § 5.2.

The geometry of the problem is a rectangular prism 2 units × 4 units in cross section and infinitely long. We solve one quadrant of the problem, and impose reflection symmetry in both x and y to represent the other three quadrants. It is assumed that the radiation freely escapes at the outside surfaces of the prism, and that no radiation impinges on the prism from outside. Calculations have been made with both ALTAIR and the Kunasz et al. code (P. Kunasz 1990, private communication) for a sequence of spatial meshes from 20 × 20 grid points up to 70 × 70 gridpoints. We compare the scattering integral $\bar{J}$ at four representative spatial points for the different meshes; the solutions are normalized to the best-resolved calculation (101 × 101), which appears to be accurate to a fraction of a percent. In Figures 6–8 we show the results for cases with $\chi_l = 10^3$ and ϵ between 10^{-1}, for which the source function is well thermalized, and 10^{-5}, for which the source function is far from being thermalized. In general, we find that at low resolution (20 × 20 to 30 × 30), ALTAIR makes errors that are less than 10% while the errors are considerably larger for the AOI treatment (greater than 20%). ALTAIR approaches the converged result more rapidly than AOI up to grids of 40 × 40. For more resolved grids, both codes are within 1% of the converged result. We also note that the convergence is most rapid for spatial points that are well removed from grid boundaries, such as point 4. The slowest spatial convergence occurs at the edges of the medium.

ALTAIR's rapid convergence with mesh size is a significant economy. Full-scale non-LTE calculations involving several thousand frequencies, several hundred levels, several hundred lines, and many time cycles are going to be computationally expensive. The results reported here indicate that ALTAIR, with discontinuous finite-element differencing, is capable of providing more accurate results with affordable meshes than AOI-type schemes.

It is interesting to study the topology of the Eddington tensors that are at the core of the tensor moment approach. In Figures 9–12 we show the "rr" component spatial distribution as a function of frequency in the line. At line center, the Eddington tensor

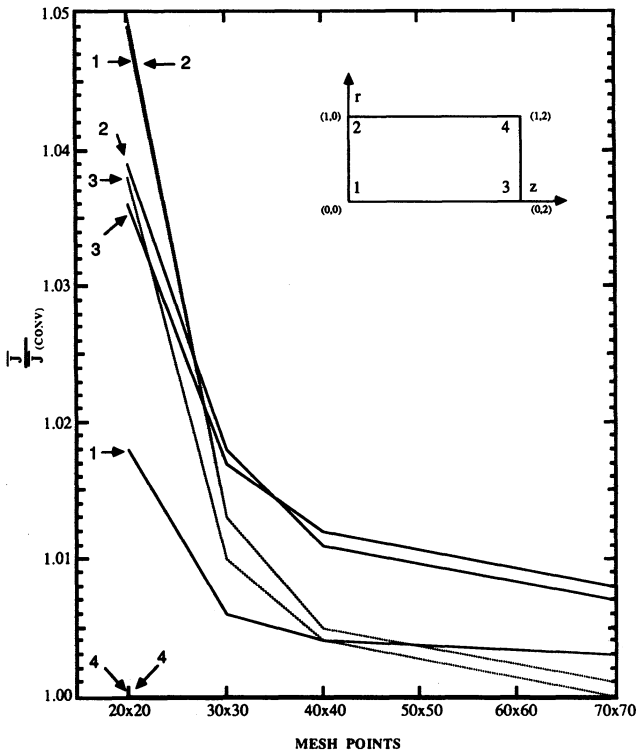

FIG. 6

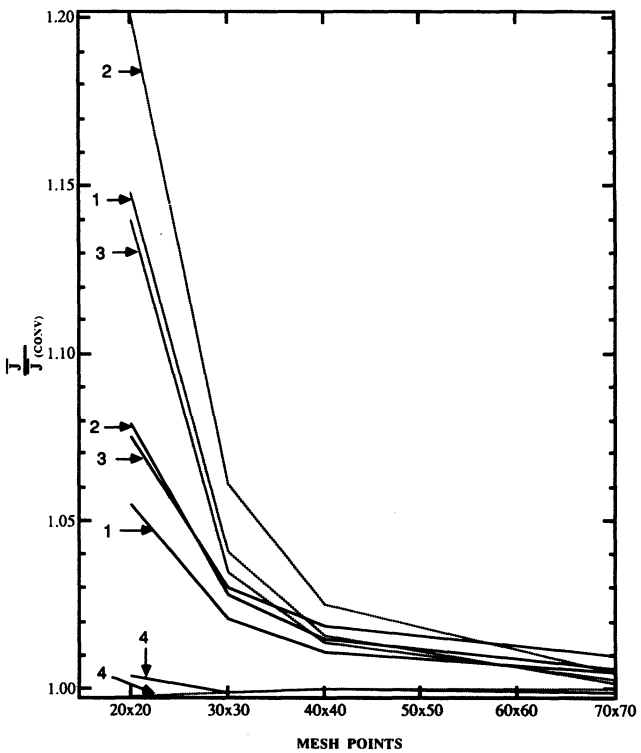

FIG. 7

FIG. 6.—Convergence comparison of the scattering integral for ALTAIR (*solid lines*) with AOI (*dashed lines*) at four different spatial points in a planar *x-y* medium as a function of grid resolution. The locations of the spatial points numbered 1–4 are indicated on the inset. This case is for a collisional thermalization parameter $\epsilon = 10^{-1}$. The source function is well thermalized.

FIG. 7.—Same as Fig. 6 with $\epsilon = 10^{-3}$. The source function is barely thermalized.

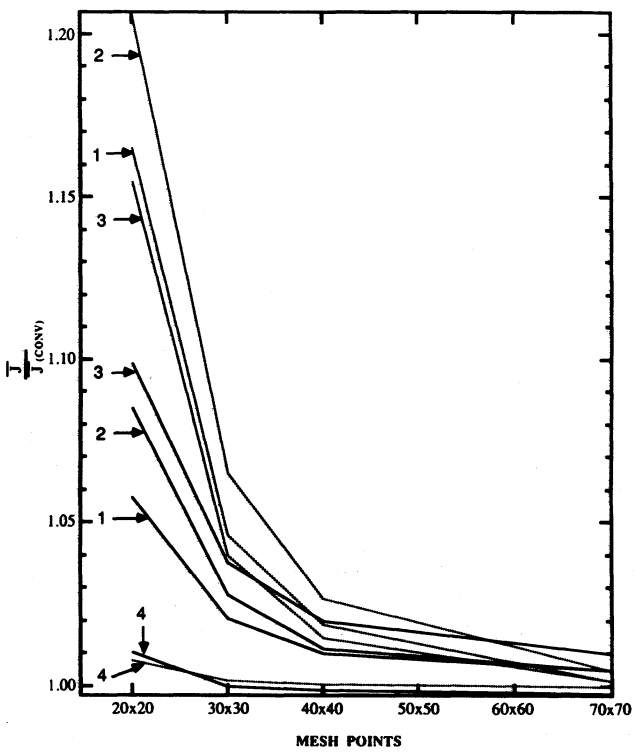

FIG. 8

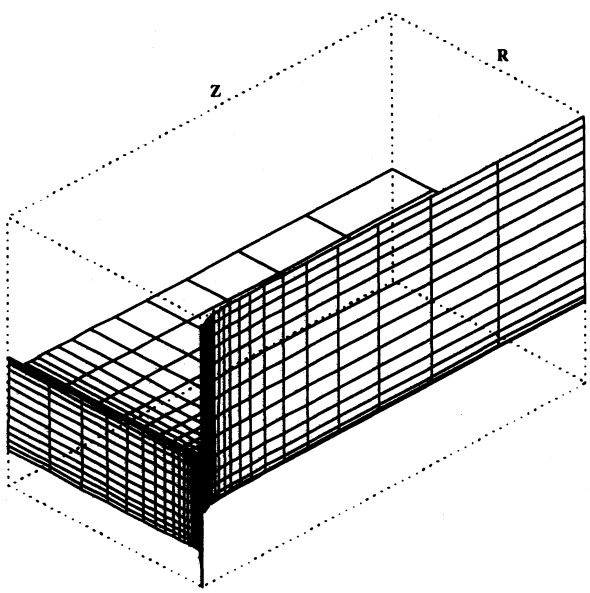

FIG. 9

FIG. 8.—Same as Fig. 6 with $\epsilon = 10^{-5}$. The source function is not thermalized.

FIG. 9.—The "*rr*" component of the Eddington tensor at line-center frequency as a function of space.

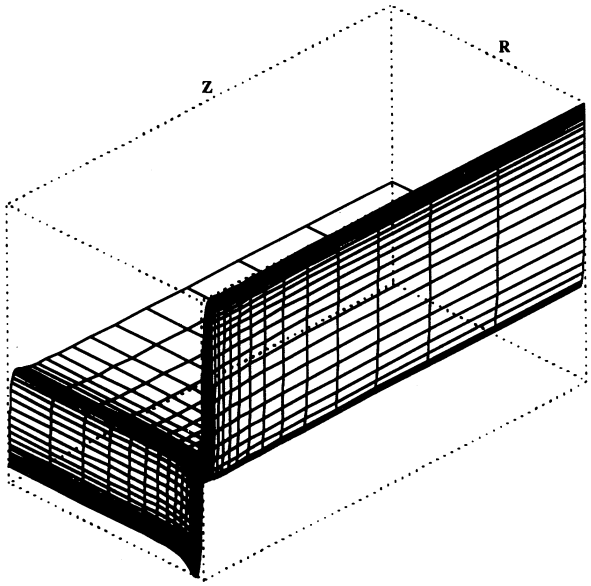

FIG. 10

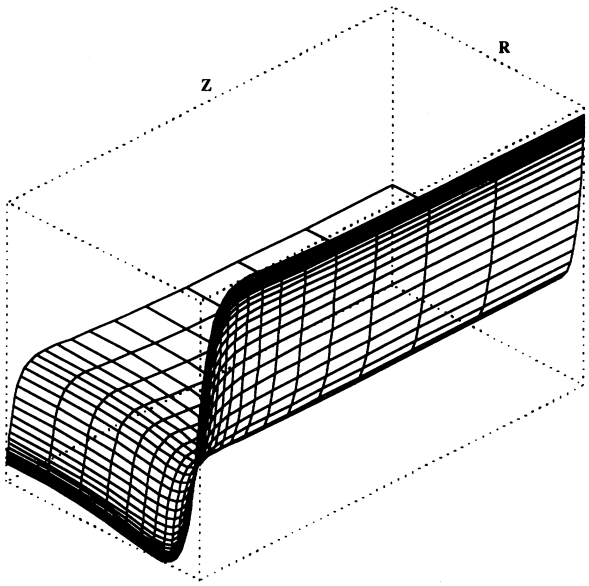

FIG. 11

FIG. 10.—The "*rr*" component of the Eddington tensor 1.5 Doppler widths from line center.
FIG. 11.—The "*rr*" component of the Eddington tensor 2.0 Doppler widths from line center.

takes on its isotropic value $\sim\frac{1}{3}$ through most of the slab but deviates from this value in the boundary layers. The boundary-layer extrema are due to the outwardly peaked intensity distribution at the surface. The tensor weighting function determines whether this extremum is a maximum or a minimum. The sharp minimum in Figure 9 is located approximately one mean free path from the corner. The nonmonotonicity of the tensor in the boundary layer is a consequence of the relative contribution of the transverse and normal components of the specific intensity. As we move away from the line center (Figs. 10–12), we note that the influence on the tensor is coming from regions removed from the boundary layer. At 1.5 Doppler widths from the line center, the medium is globally coupled, and the tensor is influenced by radiation from the entire medium. We note that the nonmonotonicity that characterized the line core boundary structure has been washed out. The "*zz*" component behaves in qualitatively the same manner. In Figure 13 we show the "*rz*" Eddington tensor component at 1.5 Doppler widths from line center. The dramatic peakedness of this function at the corner of the slab reflects the property that the angle weighting function is displaced by 45° in θ with respect to the diagonal components of the tensor.

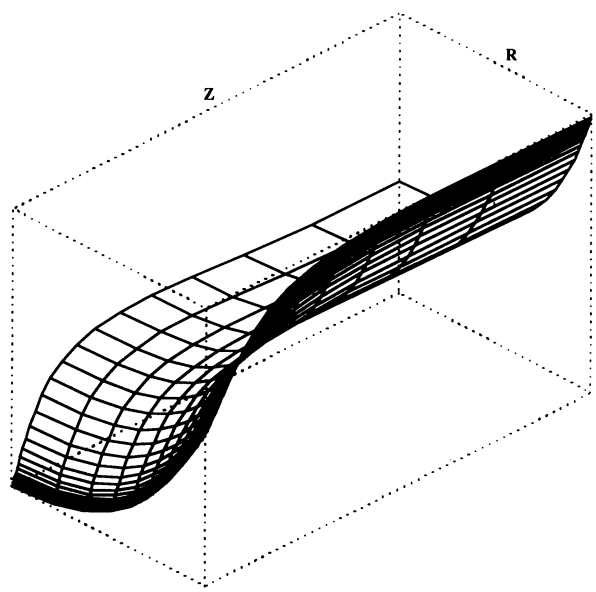

FIG. 12

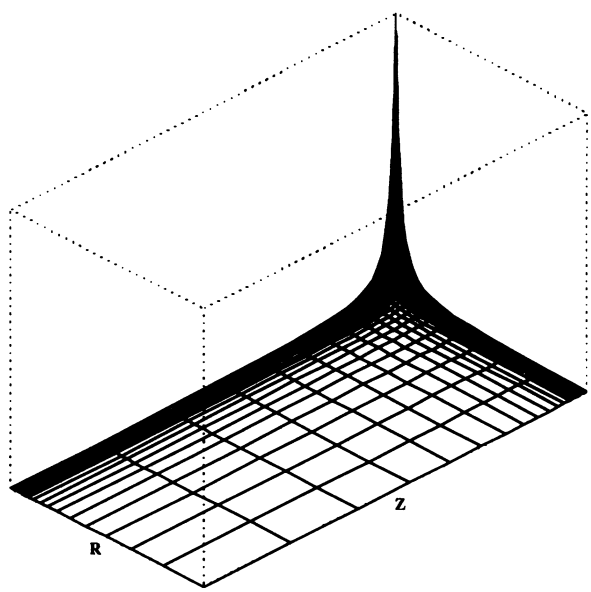

FIG. 13

FIG. 12.—The "*rr*" component of the Eddington tensor 2.5 Doppler widths from line center.
FIG. 13.—The "*rz*" component of the Eddington tensor 1.5 Doppler widths from line center.

5.2. *Nonuniform Source*

Many multidimensional astrophysical flows contain discontinuities such as shock waves or contact discontinuities. These appear as narrow regions of large gradient in the density, pressure, or temperature of the gas. A shock in an optically thick flow may greatly enhance the temperature, resulting in a strong source of thermal emission in the vicinity of the shock front. This thin, hot region may radiate in a line and give rise to a spectrum characteristic of the shock. The shock emission may modify the preshock fluid by precursor heating, as well as serving as an important spectral diagnostic. It is of interest, therefore, to assess the accuracy that can be attained in a two-dimensional radiation transport calculation for a sharply peaked thermal emission source. As a first step in this direction, we have investigated a simple problem. We assume a Planck function with a Gaussian structure along the spatial diagonal of our x-y two-dimensional grid. This loosely represents the presence of a shock in the medium. The width of the Gaussian was chosen to be $\Delta = 0.05$. Thus the value of the Planck function is unity along the diagonal and falls off as $\exp[-(l/\Delta)^2]$ for a distance l perpendicular to the diagonal. We solved this problem with grids varying from 10×10 to 60×60. For the 10×10 grid, the thermal source falls off to 3×10^{-4} within 1 grid cell away from the diagonal; thus the calculation clearly will be resolved poorly for this case. For the 60×60 model, the source falls only to 0.8; thus this case should be well resolved.

We examined both spatial and angle resolution to determine the number of grid cells and angles that would be necessary to get an accurate calcuation of the radiation field in the presence of the gradient. For the spatial resolution study, we computed the two-dimensional frequency-dependent mean intensity in a two-level atom spectral line for a range of Gaussian widths and a range of ϵ, the photon destruction probability. The results of this study are best represented by Figures 14–19. For a given value of the destruction probability ϵ, Gaussian width Δ, and frequency (either the line center or the line wing), we plot the ratio of the mean intensity for a given spatial grid to that for the spatially well-converged 100×100 grid versus grid resolution. In each case, we show the ratios for three points in the grid: point 1, the corner point of the grid at the edge of the diagonal source; point 2, the spatial midpoint on the diagonal of the thermal source; and point 3, the far corner point most distant from the thermal source. All calculations in the spatial resolution study were done with 84 rays whose chosen quadrature has been previously described.

Several conclusions can be drawn from these calculations. (1) For a given value of ϵ, the radiation field at the center of the line converges more quickly as the mesh is refined than does the radiation field in the line wing. This is because the mean free path of the photons becomes comparable, in the line wings, to the overall size of the problem, so the intensity at a given point in space will be accurate only if the transport algorithm faithfully gives the contributions to that intensity from points of emission that may be many zones away. When there is a small, hot source region, this is a severe test of the algorithm. In the line center, by contrast, the mean free path is less than the size of many of the zones, so line-center photons diffuse through the mesh; this is a benign regime for the numerical algorithm. (2) Lines with small values of ϵ are better converged for a given grid resolution. The source function is equal to

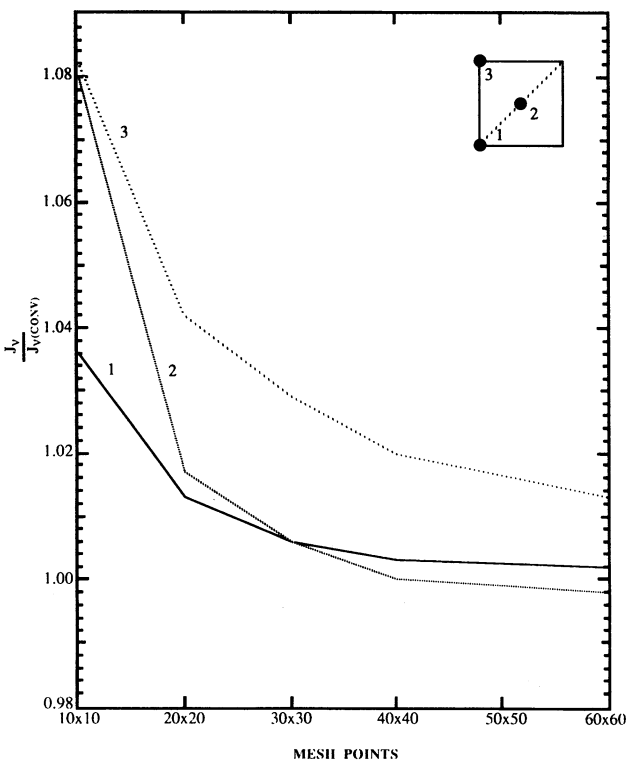

FIG. 14

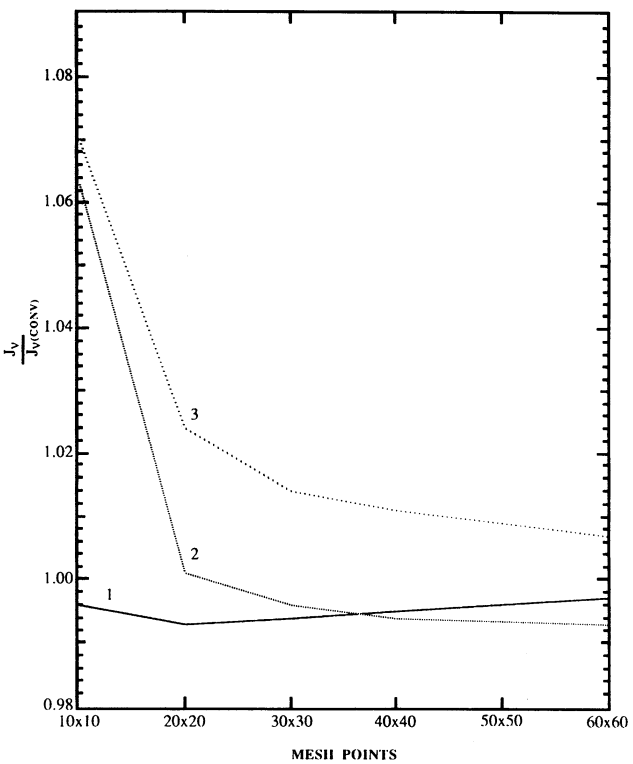

FIG. 15

FIG. 14.—Convergence of the mean intensity J_ν at line center as a function of grid resolution at three different spatial points in a grid with a Gaussian thermal source. The location of the three points with respect to the Gaussian source (*dotted line*) is shown in the inset. This case is for a collisional thermalization parameter $\epsilon = 0.5$.

FIG. 15.—Same as Fig. 14, with $\epsilon = 10^{-1}$.

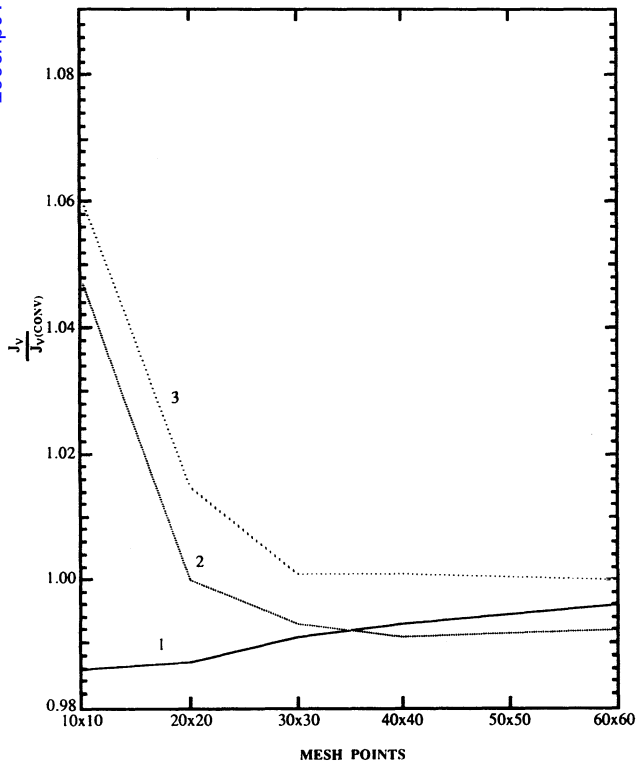

FIG. 16

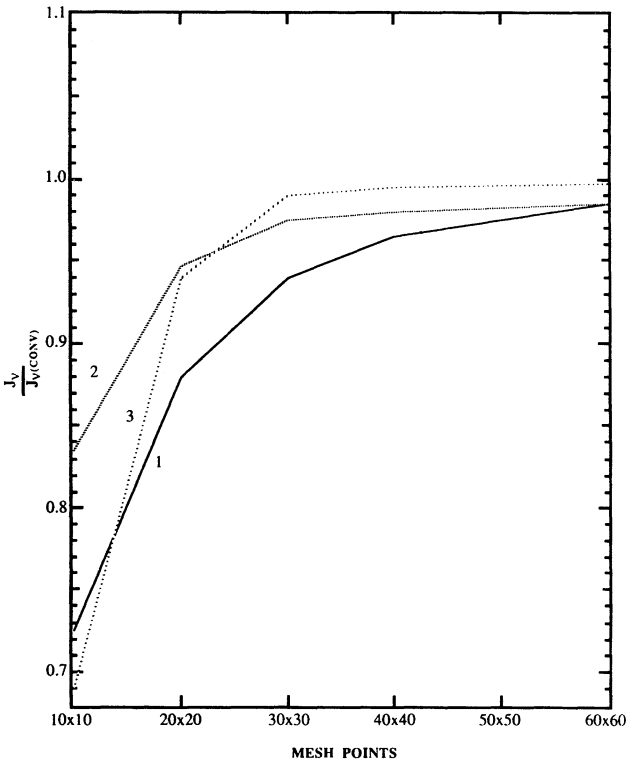

FIG. 17

FIG. 16.—Same as Fig. 14, with $\epsilon = 10^{-2}$.
FIG. 17.—Same as Fig. 14, with J_ν at the far wind frequency of the line, and $\epsilon = 0.5$.

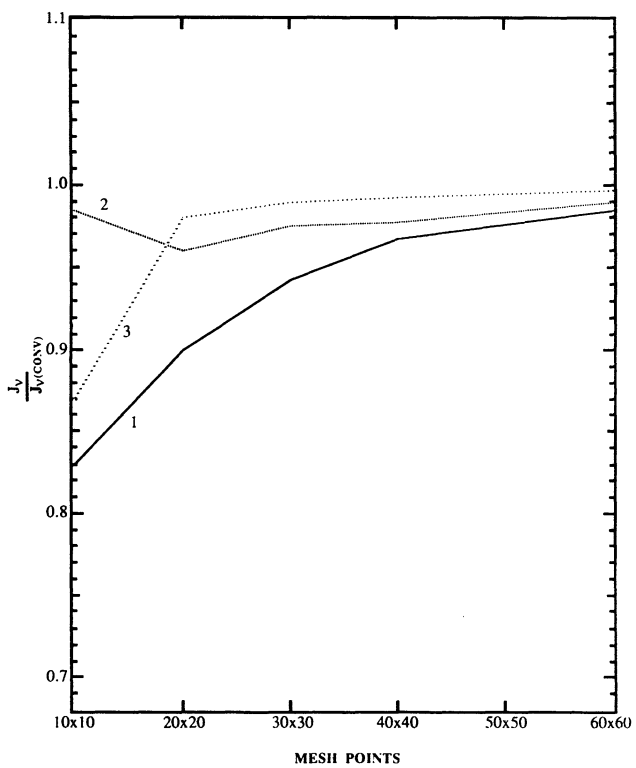

FIG. 18

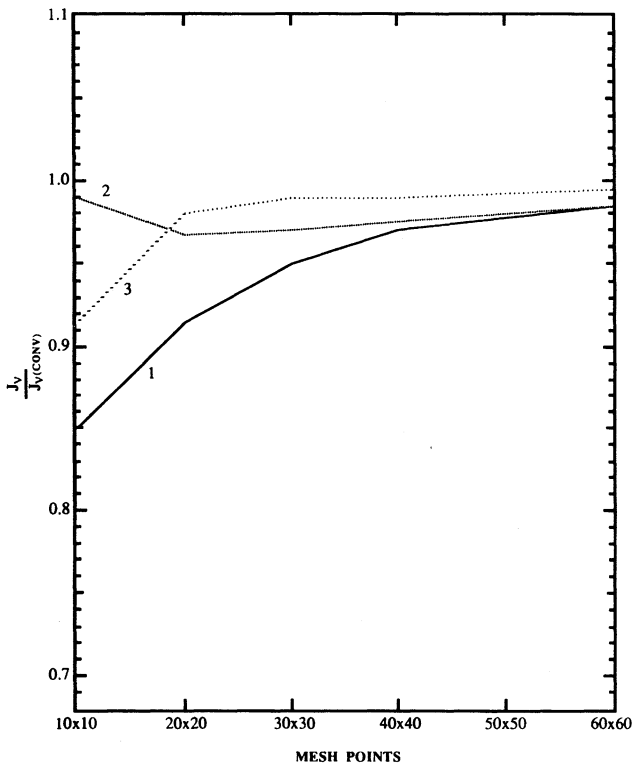

FIG. 19

FIG. 18.—Same as Fig. 17, with $\epsilon = 10^{-1}$.
FIG. 19.—Same as Fig. 17, with $\epsilon = 10^{-2}$.

the Planck function smoothed over a characteristic length, which is the thermalization length. That length is frequently much larger than the mean free path and increases as ϵ decreases. Thus, for a given distribution of the Planck function, the source function in the case of large ϵ has a sharper spatial distribution than does the source function in the small-ϵ case, with the result that the large-ϵ case is more difficult to calculate. (3) The radiation field is more difficult to resolve at corner points on the boundaries than in the interior. This is to be expected, since the intensity field is most sharply peaked in angle at the corners, which puts the maximum stress on the transport algorithm. Although structures with gradients as sharply peaked as the Gaussian studied in this example are computationally difficult to treat accurately with conventional finite-difference formulations, ALTAIR easily gets an accurate solution with relatively few grid cells using discontinuous finite-element methods. For grids with 30×30 resolution, our results indicate inaccuracies of no more than 5%. For grids with 60×60, the results are accurate to within 1%–2%.

While it is quite common for spatial resolution studies to be made of hydrodynamic as well as radiation transport calculations, far less attention has been given to the question of adequate angular resolution in radiation transport. For typical problems involving one-dimensional radiation transport, it is well known that a few angle points (typically 3–5) are all that are needed to get a highly accurate result, even in the presence of sharp gradients. This is principally because in one spatial dimension there is little tendency for sharp spatial variation of the source to induce sharp angular structure in the intensity. (An exception is the case of a thin, bright sheet, for which the intensity can be sharply peaked in the transverse direction at points within the sheet.) The situation can be drastically different in two dimensions. Here the spatial inhomogeneity leads to angular inhomogeneity, even at remote points in space. Features in two dimensions are now permitted that may need many rays to obtain an accurate representation. We must develop a knowledge base for the angular resolution that is needed to adequately represent a structure like a shock in the flow. We have examined the spatial distribution of the ratio of the mean intensity for a given angular resolution (number of rays used in the calculation) to the mean intensity for a highly resolved calculation with 220 rays (S_{20}; this number corresponds to 55 rays per octant, and 4 of the 8 octants must actually be computed). We studied the radiation field ratio for a given value of ϵ and a representative frequency in the line (line center or line wing). We find that, as in the spatial resolution study, lines that have small values of ϵ require fewer angles to treat problems with large source gradients than do the large-ϵ lines. Likewise, larger errors are found in the line wing than in the line center. For lines with large ϵ-values (0.5), errors in the radiation field in the line wing are substantial over the entire source region and can be as large as 17%–33%, if as few as 40 rays (S_8) are used in the calculation. Our calculations indicate that at least 84 rays (S_{12}) must be used in the calculation to keep the error due to angle resolution below 10%.

These preliminary studies are only an indication of the difficulties that must be faced when doing two-dimensional radiation transport in spectral lines in the presence of sharp features in the flow, such as shock waves. Clearly, high angular resolution as well as high spatial resolution is necessary in two-dimensional transport problems to obtain an accurate calculation of the spectrum of the radiation field in the presence of shocks. The problem is considerably more severe than in well-studied situations in one spatial dimension. These studies indicate an eventual need for adaptive mesh refinement in both angle and space.

5.3. *Mordant Test with Highly Distorted Mesh Structure*

The next test problem was originally used by Reed & Hill (1973) to illustrate the extraordinary stability of discontinuous finite-element representations of the transport equation when compared with first-order continuous formulations. Employing triangular zoning, they used the problem to show that the Gibbs oscillations generated in the continuous case in problems containing an internal boundary layer are virtually eliminated when the continuity requirement is relaxed. Subsequently, Mordant (1981) performed a similar comparison using both linear and bilinear rectangular elements. Since our scheme differs from Mordant's (1981) D-scheme only in our diagonalization of the source and single terms, our results are similar. The problem is specified as the superposition of two square rods. First, a long rod is defined that is one unit square and has an opacity $\chi = 1$ and a unit Planck function. Then the center section of that rod is replaced by a 0.6 unit square rod in which the opacity is $\chi = 1$, and there is no emission, $B = 0$. Thus we have a perfectly absorbing central region surrounded by a monochromatic scattering medium. The problem presents two difficulties; the intensity drops very rapidly into the cold absorber, and many numerical methods produce ringing and negative intensities (Gibbs oscillations). Also, the spatial structure of the mean intensity in the translucent material is complex, with cusps along the shadow lines.

We solve the problem in an x-y geometry, convering our axisymmetric geometry by applying an offset to the radii. We make the calculation with a fine mesh using 60×60 square zones and compare this with a calculation that uses a 20×20 mesh with severe distortions. We distort the square grid everywhere except at the region boundary, by moving each node in a randomly chosen direction. The amplitude of each displacement was chosen to be the maximum value possible, subject to the restriction that the resulting quadrilateral zones remain convex. The resulting distorted mesh is shown in Figure 20. The two calculations can be compared in Figures 21 and 22. The result of the calculation is that in neither case did the intensity go negative due to the strong absorption at the center. The agreement of the highly distorted coarse mesh calculation and the regular mesh fine zone calculation is remarkable and is of the order of 2%, except just inside the absorber. In Figure 23 we superpose a three-dimensional representation of the low-resolution irregular calculation over the regular high-resolution calculation to illustrate the excellent agreement. This highly desirable behavior of the numerical solution comes about as a result of our mass grouping modification to the DFE representation, which gives a strictly monotone decrease in the mean intensity as the center of the two rods is approached. Our results indicate that, with our formulation, it is possible to get accurate results to complex multi-dimensional transfer problems with few spatial zones, even in distances where highly distorted zones must be used to model a particular geometry.

5.4. *Line Formation in a Cylinder*

Many problems of astrophysical interest involve the transfer of radiation in an accretion disk. This problem is inherently two-dimensional. Here we discuss the related problem of the formation of a spectral line with complete redistribution by a uniform cylinder of conservatively scattering material. We can specify the problem by assuming complete redistribution with a Doppler line

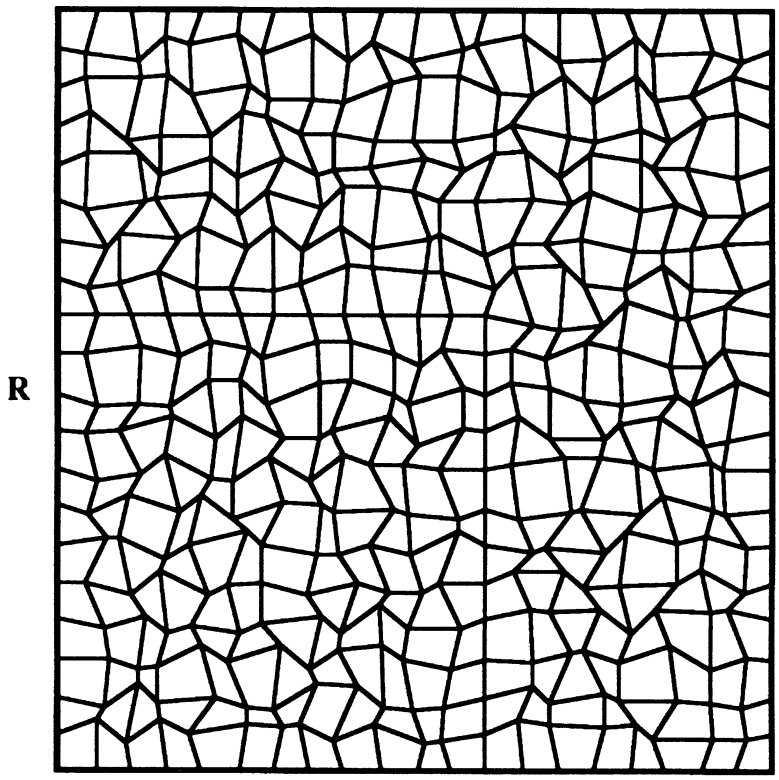

FIG. 20.—Distorted mesh on a 20 × 20 grid for the Mordant test problem.

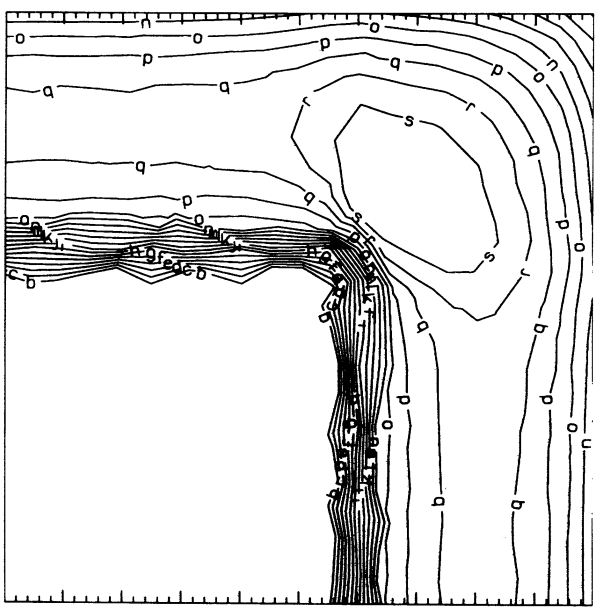

FIG. 21

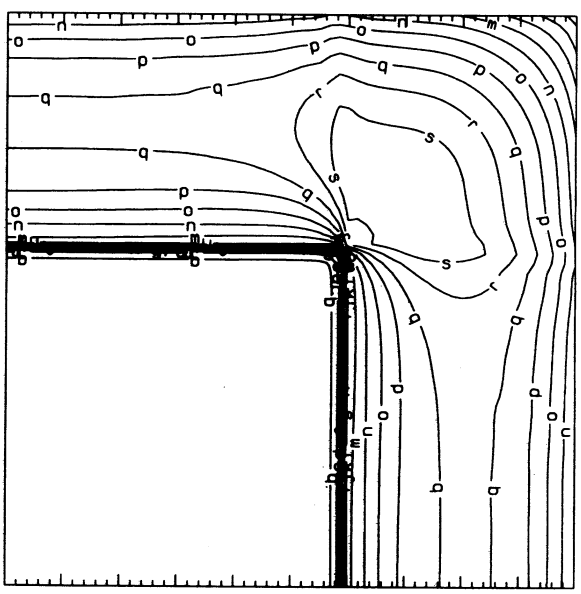

FIG. 22

FIG. 21.—Contours for the mean intensity J for the Mordant test problem. One quadrant of the problem is shown. The contour interval is $0.05J_{max}$. Distorted 20 × 20 mesh.

FIG. 22.—Same as Fig. 21, with unifrom 60 × 60 mesh.

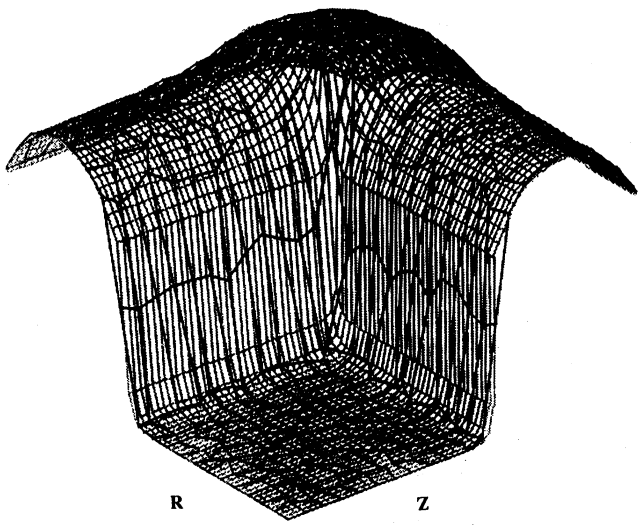

FIG. 23

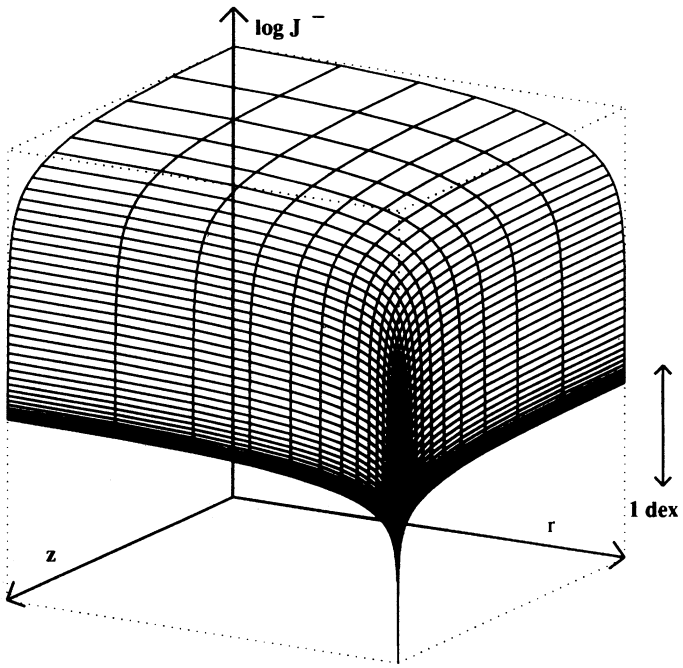

FIG. 24

FIG. 23.—Three-dimensional representation of the spatial dependence of the mean intensity for the Mordant test problem with mean intensity for the distorted mesh calculation superposed on the mean intensity for the uniform mesh. The actual mesh lines are indicated on the surface. Note the excellent agreement in the results.

FIG. 24.—Perspective plot of $\bar{J}$, on a logarithmic scale, vs. location in the equal dimension cylinder ($D = L$). The actual mesh lines are indicated on the surface. The arrow shows the extent of one decade on the vertical axis.

profile. In this problem, the optical depth across the diameter or along the length, whichever is less (integrated over the frequency in Doppler units), is fixed at 2×10^4. We vary the diameter/length from 0.1 to 10 to illustrate the effects of scattering of radiation in structures that vary from filaments to spheres to disks. We assume conservative scattering ($\epsilon = 0$) and a uniform source of line photons in the cylinder. One of the main quantities of interest that can be derived from the solution of these problems is $\langle N \rangle$, the mean number of scatterings of line photons in escaping the cylinder. If s is the contribution to the source function from the primary source of photons, then the expression for $\langle N \rangle$ is $\int \chi S\, dV / \int \chi s\, dV$. Analytic work by Ivanov (1973) has shown that $\langle N \rangle$ increases in proportion to the optical depth for a Doppler line profile. Our present calculations show the manner in which $\langle N \rangle$ varies with the aspect ratio of the cylinder. These calculations have used a 40×40 spatial mesh and the S_{20} angle set. Several of the quantities of interest are given in Table 1. We have also included analytic results for $\langle N \rangle$ for the cases of the one-dimensional slab and sphere in Table 1.

We note that the mean number of scatterings varies relatively little among cylinders of varying aspect ratio that have the smallest dimension. Analytic results from Ivanov (1973) are shown in Table 1 for the mean number of scatterings in the one-dimensional slab, which should agree with the limiting cylinder $D \gg L$, and in the one-dimensional sphere, which is approximated by $D = L$. Also shown are the fraction of photons that escape through the curved sides of the cylinder and the values of $\bar{J}$ at the center, the middle of a circular enclosure, and the corner of the cylinder. We note a great contrast between the corner and top side value of $\bar{J}$. It suggests that $\bar{J}_{\rm top/s}$ scales as $O(\tau^{1/2})$, while $\bar{J}_{\rm cor/s}$ scales as $O(1)$. The very small value of J near the corner is confined to a region that is only one mean free path in extent. This is illustrated in Figure 24.

TABLE 1

UNIFORM CYLINDER RESULTS

χD	χL	F(side)/F	$\langle N \rangle$	$\bar{J}_{\rm c/s}$	$\bar{J}_{\rm top/s}$	$\bar{J}_{\rm cor/s}$
2×10^5	2×10^4	0.125	4.66×10^4	6.66×10^4	3.27×10^2	8.04
10^5	2×10^4	0.236	4.18	6.54	3.24	7.85
4×10^4	2×10^4	0.479	3.06	5.46	2.82	7.31
2×10^4	2×10^4	0.686	2.00	3.70	2.08	6.53
2×10^4	4×10^4	0.834	2.36	4.16	2.16	6.61
2×10^4	10^5	0.933	2.58	4.24	2.16	6.62
2×10^4	2×10^5	0.966	2.66	4.24	2.16	6.62

NOTE.—Analytic results for $\langle N \rangle$: 5.3×10^4 (one-dimensional slab), 1.9×10^4 (one-dimensional sphere).

6. CONCLUSIONS

We have developed a new code, ALTAIR, that solves the time-dependent non-LTE problem for a multilevel atom in two-dimensional axisymmetric geometry on a Lagrangian mesh of arbitrary complexity. We employ a new generalization of the variable Eddington factor method in one dimension to a combined variable tensor method for both x-y and r-z geometries in two dimensions. The generalized combined tensor factor method requires the solution in two dimensions of both the full transport equations and the tensor moment equations on a logical mesh of convex quadrilateral zones. We describe in detail the double-splitting iteration acceleration procedure we employ to solve the tensor moment equations. To solve the transport equation, we introduce a modified DFE method. Although finite-element schemes have been used for several years in neutron transport theory, they are just beginning to surface in photon transport. Our modification to radiation transport is to mass lump the time evolution, emission, and absorption terms. We achieve a scheme that is highly stable under conditions of large zone-to-zone variation in sources and opacities. These conditions can be expected in many problems of astrophysical interest. We develop for the first time a completely self-consistent formulation of the moment equations, with the radiation transport equation for which exact agreement of the transport and moment energies is ensured. The discretization of the tensor moment equations employs a continuous finite-element formulation. We describe a set of test problems in two-dimensional transfer which show the power of our new approach. These calculations demonstrate the excellent convergence properties as well as the accuracy of our finite-element tensor approach. A fundamental limitation of the generalized Eddington tensor approach appears to be its restriction to either stationary or very low velocity flows. The introduction of a preferred direction through the presence of a spatially varying velocity field renders the opacity anisotropic. As a result, the formulation of the zeroth and first moments of the transport equation yield opacity-weighted moments of the specific intensity which do not naturally lend themselves to the construction of a combined tensor moment equation. Such an equation, however, can be constructed but has a certain degree of arbitrariness associated with it in the choice of the fundamental degree of freedom analogous to the mean intensity. Our experiments with such a combined moment equation lead us to doubt that a robust convergence can be obtained. Our experience indicates that the presence of even a small velocity-field–induced frequency shift in a line produces noticeable increases in the number of iterations necessary for a converged result. No such difficulties arise for stationary calculations. In future work, we will introduce a new multigrid angle perturbation method that allows arbitrarily large velocity fields with no substantial increase in the number of iterations required for convergence. Our ability to solve radiation transfer problems in two dimensions on an arbitrary Lagrangian mesh allows problems involving complicated disk geometries prevalent in a wide variety of astrophysical phenomena to be handled with ease.

We acknowledge several useful discussions with David Levermore on the use of tensor moments, and discussions with Gordon Olson, Larry Auer, and Paul Kunasz on multidimensional radiative transfer at early stages in this work. We express gratitude to Paul Kunasz for the use of his AOI code with which to make detailed comparisons with ALTAIR. The computations were carried out on the YMP8/128 supercomputer at Lawrence Livermore National Laboratory. This work was performed in part under the auspices of the US Department of Energy at the Lawrence Livermore National Laboratory under contract W-7405-ENG-48.

APPENDIX A

TRIANGLE AVERAGE OF A LINEAR FUNCTION $G(r, z)$

The volume average over the typical triangle 012 in Figure 2 of a general linear function $G(r, z)$ is given by

$$(G)_{012} = \frac{2\pi}{V_{012}} \int_{012} G(r, z) r \, dr \, dz = \frac{2\pi}{V_{012}} \sum_{n=0}^{2} G_n \int_{012} w_n r \, dr \, dz = \frac{1}{V_{012}} \sum_{n=0}^{2} G_n V_n , \tag{A1}$$

where V_{012} is the volume of rotation of triangle 012 about the z-axis given by equation (4.2), and V_n is that portion of V_{012} associated with node n according to equation (4.8). We shall also need

$$\left(\frac{G}{r}\right)_{012} = \frac{2\pi}{V_{012}} \int_{012} \frac{G}{r} r \, dr \, dz = \frac{2\pi}{V_{012}} \int_{012} G \, dr \, dz = \frac{2\pi}{V_{012}} \sum_{n=0}^{2} G_n \int_{012} w_n \, dr \, dz . \tag{A2}$$

The area integral of the basis function w_n can be obtained from the volume integral of the same function, since the r-dependence in equation (4.7) is explicit. Setting $\bar{r}_{012} = r_n = 1$ in that equation gives

$$2\pi \int_{012} w_n \, dr \, dz = \tfrac{2}{3}\pi A_{012}, \tag{A3}$$

so that equation (A2) becomes

$$\left(\frac{G}{r}\right)_{012} = \frac{1}{V_{012}} \frac{2\pi}{3} A_{012} \sum_{n=0}^{2} G_n = \frac{1}{\bar{r}_{012}} \frac{1}{3} \sum_{n=0}^{2} G_n = \frac{\bar{G}_{012}}{\bar{r}_{012}} , \tag{A4}$$

where we have used equation (4.2) and defined

$$\bar{G}_{012} = \tfrac{1}{3}(G_0 + G_1 + G_2) . \tag{A5}$$

Equation (A3) displays the property of the basis functions that they define equal-area weights on the triangle. The partial derivatives of G with respect to r and z will be needed as well. They are especially simple since they are constants; by inspection of the definitions in equation (4.4),

$$\left(\frac{\partial}{\partial r} G\right)_{012} = \sum_{n=0}^{2} G_n \frac{\partial w_n}{\partial r} = \frac{1}{2A_{012}} [G_0(z_2 - z_1) + G_1(z_0 - z_2) + G_2(z_1 - z_0)] \tag{A6a}$$

and

$$\left(\frac{\partial}{\partial z} G\right)_{012} = -\frac{1}{2A_{012}} [G_0(r_2 - r_1) + G_1(r_0 - r_2) + G_2(r_1 - r_0)] . \tag{A6b}$$

APPENDIX B

PROPERTIES OF BILINEAR ELEMENTS ON QUADRILATERALS

As implemented in ALTAIR, the approximate numerical solution to the discretized version of the radiation transport equation (2.1) is represented by bilinear finite elements on the quadrilateral zones. Let (r_l, z_l), $l = 1, 2, 3, 4$, be the spatial coordinates of the vertices, or nodes, of a given zone. The bilinearity will actually be in terms of local coordinates α and β on the unit square: $0 \leq \alpha, \beta \leq 1$. A bilinear mapping of the unit square onto the quadrilateral zone is then defined by

$$r = \sum_{l=1}^{4} w_l r_l , \qquad z = \sum_{l=1}^{4} w_l z_l , \tag{B1}$$

where

$$w_1 = (1 - \alpha)(1 - \beta) , \qquad w_2 = (1 - \alpha)\beta , \qquad w_3 = \alpha\beta \tag{B2}$$

and

$$w_4 = \alpha(1 - \beta) .$$

A typical quadrilateral zone is shown in Figure 1.

The w_l functions constitute a basis for the space of bilinear shape functions on the unit square. They have the property that

$$w_k(r_l, z_l) = \delta_{kl} , \qquad k, l = 1, 2, 3, 4 , \tag{B3}$$

and the completeness relation

$$\sum_{l=1}^{4} w_l(r, z) = 1 \tag{B4}$$

for points (r, z) within the quad (cf. equations [4.5] and [4.6]).

Taking the differentials of the map in equation (B1) for the arbitrary but specific quadrilateral zone shown in Figure 1 and denoting

$$\Delta r = r_1 + r_3 - r_2 - r_4 , \qquad \Delta z = z_1 + z_3 - z_2 - z_4 \tag{B5}$$

gives

$$dr = f_r d\alpha + g_r d\beta , \qquad dz = f_z d\alpha + g_z d\beta , \tag{B6}$$

where

$$\frac{\partial r}{\partial \alpha} = f_r = r_4 - r_1 + \beta\Delta r , \qquad \frac{\partial r}{\partial \beta} = g_r = r_2 - r_1 + \alpha\Delta r , \qquad \frac{\partial z}{\partial \alpha} = f_z = z_4 - z_1 + \beta\Delta z ,$$

and

$$\frac{\partial z}{\partial \beta} = g_z = z_2 - z_1 + \alpha\Delta z . \tag{B7}$$

The inverse relations follow from equation (B6):

$$d\alpha = \frac{1}{f_r g_z - f_z g_r} (g_z dr - g_r dz) , \qquad d\beta = \frac{1}{f_r g_z - f_z g_r} (-f_z dr + f_r dz) , \tag{B8}$$

so that

$$\frac{\partial \alpha}{\partial r} = \frac{g_z}{f_r g_z - f_z g_r} , \qquad \frac{\partial \beta}{\partial r} = -\frac{f_z}{f_r g_z - f_z g_r} , \qquad \frac{\partial \alpha}{\partial z} = -\frac{g_r}{f_r g_z - f_z g_r} ,$$

and

$$\frac{\partial\beta}{\partial z}=\frac{f_r}{f_r g_z - f_z g_r}\,. \tag{B9}$$

Expressions for the r and z derivatives of a general bilinear function G defined by equation (3.1) will be needed. We have

$$\frac{\partial G}{\partial r}=\frac{\partial G}{\partial\alpha}\frac{\partial\alpha}{\partial r}+\frac{\partial G}{\partial\beta}\frac{\partial\beta}{\partial r}\,.$$

By comparison with equation (B7),

$$\frac{\partial G}{\partial\alpha}=f_G=G_4-G_1+\beta\Delta G \qquad \text{and} \qquad \frac{\partial G}{\partial\beta}=g_G=G_2-G_1+\alpha\Delta G\,, \tag{B10}$$

where

$$\Delta G=G_1+G_3-G_2-G_4\,. \tag{B11}$$

Thus,

$$\frac{\partial G}{\partial r}=f_G\frac{\partial\alpha}{\partial r}+g_G\frac{\partial\beta}{\partial r}=\frac{f_G g_z - f_z g_G}{f_r g_z - f_z g_r}\,. \tag{B12}$$

Likewise,

$$\frac{\partial G}{\partial z}=f_G\frac{\partial\alpha}{\partial z}+g_G\frac{\partial\beta}{\partial z}=\frac{f_r g_G - f_G g_r}{f_r g_z - f_z g_r}\,. \tag{B13}$$

An oriented element of cross-sectional area on the quad is given by

$$\boldsymbol{dS}=\boldsymbol{dz}\times\boldsymbol{dr}=(f_r g_z - f_z g_r)\boldsymbol{d\beta}\times\boldsymbol{d\alpha}\,, \tag{B14}$$

where, from their definitions in equation (B7),

$$f_r g_z - f_z g_r=(r_4-r_1)(z_2-z_1)-(r_2-r_1)(z_4-z_1)+[(r_4-r_1)\Delta z-(z_4-z_1)\Delta r]\alpha+[(z_2-z_1)\Delta r-(r_2-r_1)\Delta z]\beta\,. \tag{B15}$$

The cross-sectional area of a zone is then

$$\Sigma=\int d\Sigma=\iint_0^1 d\alpha\,d\beta\,(f_r g_z - f_z g_r)=\tfrac{1}{2}[(z_3-z_1)(r_4-r_2)+(z_4-z_2)(r_1-r_3)]\,. \tag{B16}$$

Equation (B16) and every other integral that we shall need can be obtained as a special case of the following general result. If G and H are general bilinear forms on the zone, and $d\Sigma$ is the area element in equation (B14), then

$$2\pi\int d\Sigma\,GH=\frac{\pi}{36}\{\lambda[(z_3-z_1)(r_4-r_2)+(z_4-z_2)(r_1-r_3)]+\rho[(r_4-r_1)\Delta z-(z_4-z_1)\Delta r]+\sigma[(z_2-z_1)\Delta r-(r_2-r_1)\Delta z]\}\,, \tag{B17}$$

where

$$\lambda(G,H)=\lambda(H,G)=G_1(4H_1+2H_2+H_3+2H_4)+G_2(2H_1+4H_2+2H_3+H_4)+G_3(H_1+2H_2+4H_3+2H_4)+G_4(2H_1+H_2+2H_3+4H_4)\,, \tag{B18}$$

$$\rho(G,H)=\rho(H,G)=-G_1(2H_1+H_2)-G_2(H_1+2H_2)+G_3(2H_3+H_4)+G_4(H_3+2H_4)\,, \tag{B19}$$

and

$$\sigma(G,H)=\sigma(H,G)=-G_1(2H_1+H_4)+G_2(2H_2+H_3)+G_3(H_2+2H_3)-G_4(H_1+2H_4)\,. \tag{B20}$$

The zone area follows from (equation B17) when $G=1/2\pi$ and $H=1$. Its volume of revolution about the z-axis is obtained by setting $G=r$ and $H=1$:

$$V=2\pi\iint_0^1 d\alpha\,d\beta\,(f_r g_z - f_z g_r)r\,. \tag{B21}$$

The fraction V_l of V associated with vertex l is defined by equation (3.10) and obtained from equation (B17) with $G=r$, $H=w_l$:

$$V_l=2\pi\iint_0^1 d\alpha\,d\beta\,(f_r g_z - f_z g_r)rw_l\,. \tag{B22}$$

APPENDIX C

REDUCTION OF EQUATIONS

The spatial integrals in equations (B21), (B22), and (3.12)–(3.14) that appear in the matrix representation in equation (3.11) of the transport operator on a quadrilateral zone are evaluated below in terms of cylindrical coordinates. The node numbers $k, l = 1, 2, 3, 4$ refer to Figure 1. Let

$$\Delta r_{kl} = r_k - r_l\,, \qquad \Delta z_{1l} = z_k - z_l\,, \qquad a = 4r_1 + 2r_2 + r_3 + 2r_4\,, \qquad b = 2r_1 + 4r_2 + 2r_3 + r_4\,,$$
$$c = r_1 + 2r_2 + 4r_3 + 2r_4\,, \qquad d = 2r_1 + r_2 + 2r_3 + 4r_4\,, \qquad e = \Delta z_{31}\Delta r_{42} + \Delta z_{42}\Delta r_{13}\,,$$
$$f = \Delta r_{41}\Delta z - \Delta z_{41}\Delta r\,, \quad \text{and} \quad g = \Delta z_{21}\Delta r - \Delta r_{21}\Delta z\,,$$

where

$$\Delta r = r_1 + r_3 - r_2 - r_4 \quad \text{and} \quad \Delta z = z_1 + z_3 - z_2 - z_4\,.$$

Then the vertex volumes in equation (B22) are

$$V_1 = \frac{\pi}{36}\,[ae - (2r_1 + r_2)f - (2r_1 + r_4)g]\,, \qquad V_2 = \frac{\pi}{36}\,[be - (r_1 + 2r_2)f + (2r_2 + r_3)g]\,,$$

$$V_3 = \frac{\pi}{36}\,[ce + (2r_3 + r_4)f + (r_2 + 2r_3)g]\,, \quad \text{and} \quad V_4 = \frac{\pi}{36}\,[de + (r_3 + 2r_4)f - (r_1 + 2r_4)g]\,.$$

The sum of the V_l is the quad volume in equation (B21):

$$V = \frac{\pi}{4}\left[(r_1 + r_2 + r_3 + r_4)e + \frac{1}{3}(r_3 + r_4 - r_1 - r_2)f + \frac{1}{3}(r_2 + r_3 - r_1 - r_4)g\right].$$

The z-direction transport terms in equation (3.12) are

$$(I\,\partial_z w_1) = \frac{\pi}{36}\,\{I_1[a\Delta r_{24} - (2r_1 + r_2)\Delta r_{32} - (2r_1 + r_4)\Delta r_{43}] + I_2[b\Delta r_{24} - (r_1 + 2r_2)\Delta r_{32} + (2r_2 + r_3)\Delta r_{43}]$$
$$+ I_3[c\Delta r_{24} + (2r_3 + r_4)\Delta r_{32} + (r_2 + 2r_3)\Delta r_{43}] + I_4[d\Delta r_{24} + (r_3 + 2r_4)\Delta r_{32} - (r_1 + 2r_4)\Delta r_{43}]\}\,,$$

$$(I\,\partial_z w_2) = \frac{\pi}{36}\,\{I_1[a\Delta r_{31} - (2r_1 + r_2)\Delta r_{14} - (2r_1 + r_4)\Delta r_{34}] + I_2[b\Delta r_{31} - (r_1 + 2r_2)\Delta r_{14} + (2r_2 + r_3)\Delta r_{34}]$$
$$+ I_3[c\Delta r_{31} + (2r_3 + r_4)\Delta r_{14} + (r_2 + 2r_3)\Delta r_{34}] + I_4[d\Delta r_{31} + (r_3 + 2r_4)\Delta r_{14} - (r_1 + 2r_4)\Delta r_{34}]\}\,,$$

$$(I\,\partial_z w_3) = \frac{\pi}{36}\,\{I_1[a\Delta r_{42} - (2r_1 + r_2)\Delta r_{41} - (2r_1 + r_4)\Delta r_{12}] + I_2[b\Delta r_{42} - (r_1 + 2r_2)\Delta r_{41} + (2r_2 + r_3)\Delta r_{12}]$$
$$+ I_3[c\Delta r_{42} + (2r_3 + r_4)\Delta r_{41} + (r_2 + 2r_3)\Delta r_{12}] + I_4[d\Delta r_{42} + (r_3 + 2r_4)\Delta r_{41} - (r_1 + 2r_4)\Delta r_{12}]\}\,,$$

and

$$(I\,\partial_z w_4) = \frac{\pi}{36}\,\{I_1[a\Delta r_{13} - (2r_1 + r_2)\Delta r_{23} - (2r_1 + r_4)\Delta r_{21}] + I_2[b\Delta r_{13} - (r_1 + 2r_2)\Delta r_{23} + (2r_2 + r_3)\Delta r_{21}]$$
$$+ I_3[c\Delta r_{13} + (2r_3 + r_4)\Delta r_{23} + (r_2 + 2r_3)\Delta r_{21}] + I_4[d\Delta r_{13} + (r_3 + 2r_4)\Delta r_{23} - (r_1 + 2r_4)\Delta r_{21}]\}\,.$$

The r-direction transport terms are given by equation (3.13). They can be obtained directly from the $(I\,\partial_z w_l)$ terms by making the substitution $\Delta r_{kl} \rightarrow \Delta z_l k$:

$$(I\,\partial_r w_1) = 1\frac{\pi}{36}\,\{I_1[a\Delta z_{42} - (2r_1 + r_2)\Delta z_{23} - (2r_1 + r_4)\Delta z_{34}] + I_2[b\Delta z_{42} - (r_1 + 2r_2)\Delta z_{23} + (2r_2 + r_3)\Delta z_{34}]$$
$$+ I_3[c\Delta z_{42} + (2r_3 + r_4)\Delta z_{23} + (r_2 + 2r_3)\Delta z_{34}] + I_4[d\Delta z_{42} + (r_3 + 2r_4)\Delta z_{23} - (r_1 + 2r_4)\Delta z_{34}]\}\,,$$

$$(I\,\partial_r w_2) = \frac{\pi}{36}\,\{I_1[a\Delta z_{13} - (2r_1 + r_2)\Delta z_{41} - (2r_1 + r_4)\Delta z_{43}] + I_2[b\Delta z_{13} - (r_1 + 2r_2)\Delta z_{41} + (2r_2 + r_3)\Delta z_{43}]$$
$$+ I_3[c\Delta z_{13} + (2r_3 + r_4)\Delta z_{41} + (r_2 + 2r_3)\Delta z_{43}] + I_4[d\Delta z_{13} + (r_3 + 2r_4)\Delta z_{41} - (r_1 + 2r_4)\Delta z_{43}]\}\,,$$

$$(I\,\partial_r w_3) = \frac{\pi}{36}\,\{I_1[a\Delta z_{24} - (2r_1 + r_2)\Delta z_{14} - (2r_1 + r_4)\Delta z_{21}] + I_2[b\Delta z_{24} - (r_1 + 2r_2)\Delta z_{14} + (2r_2 + r_3)\Delta z_{21}]$$
$$+ I_3[c\Delta z_{24} + (2r_3 + r_4)\Delta z_{14} + (r_2 + 2r_3)\Delta z_{21}] + I_4[d\Delta z_{24} + (r_3 + 2r_4)\Delta z_{14} - (r_1 + 2r_4)\Delta z_{21}]\}\,,$$

and

$$(I\,\partial_r w_4) = \frac{\pi}{36}\{I_1[a\Delta z_{31} - (2r_1 + r_2)\Delta z_{32} - (2r_1 + r_4)\Delta z_{12}] + I_2[b\Delta z_{31} - (r_1 + 2r_2)\Delta z_{32} + (2r_2 + r_3)\Delta z_{12}]$$
$$+ I_3[c\Delta z_{31} + (2r_3 + r_4)\Delta z_{32} + (r_2 + 2r_3)\Delta z_{12}] + I_4[d\Delta z_{31} + (r_3 + 2r_4)\Delta z_{32} - (r_1 + 2r_4)\Delta z_{12}]\} .$$

The angle transport terms in equation (3.14) are

$$\left(\frac{Iw_1}{r}\right) = \frac{\pi}{36}[I_1(4e - 2f - 2g) + I_2(2e - f) + I_3 e + I_4(2e - g)] ,$$

$$\left(\frac{Iw_2}{r}\right) = \frac{\pi}{36}[I_1(2e - f) + I_2(4e - 2f + 2g) + I_3(2e + g) + I_4 e] ,$$

$$\left(\frac{Iw_3}{r}\right) = \frac{\pi}{36}[I_1 e + I_2(2e + g) + I_3(4e + 2f + 2g) + I_4(2e + f)] ,$$

and

$$\left(\frac{Iw_4}{r}\right) = \frac{\pi}{36}[I_1(2e - g) + I_2 e + I_3(2e + f) + I_4(4e + 2f - 2g)] .$$

REFERENCES

Auer, L. H., & Mihalas, D. 1970, MNRAS, 149, 60
Cannon, C. J., & Rees, D. E., 1971, ApJ, 169, 157
Castor, J. I., Dykema, P., & Klein, R. I. 1991, in Stellar Atmospheres: Beyond Classical Models, ed, L. Crivellari, I. Hubeny, & D. G. Hummer (Dordrecht: Kluwer), 49
———. 1992, ApJ, 387, 561 (Paper II)
Feautrier, P. 1964, C. R. Acad. Sci. Paris, 258, 3189
Goldin, V. Ya. 1964, USSR Comp. Math. and Math. Phys., 4, 136
Hageman, L. A., & Young, D. M. 1981, Applied Iterative Methods (New York: Academic)
Ivanov, V. V. 1973, Transfer of Radiation in Spectral Lines, trans. D. G. Hummer, US Department of Commerce, Washington, DC
Klein, R. I., Castor, J. I., Greenbaum, A., Taylor, D., & Dukema, P. 1989, J. Quant. Spectrosc. Radiat. Transfer, 41, 199 (Paper I)
Kunasz, P. B., & Olson, G. L. 1988, J. Quant. Spectrosc. Radiat. Transfer, 39, 1
Mihalas, D. 1978, Stellar Atmospheres (2d ed.; San Francisco: Freeman)
Mihalas, D., Auer, L. H., & Mihalas, B. 1978, ApJ, 220, 1001
Mihalas, D., & Klein, R. I. 1982, J. Comput. Phys., 46, 97
Mihalas, D., & Mihalas, B. 1984, Foundations of Radiation Hydrodynamics (New York: Oxford Univ. Press)
Mordant, M. 1975, paper presented to IAEA meeting, Bologna, Italy, November 3–5
———. 1976, paper presented to ANS-ENS conf., Washington, DC, November 14–19
———. 1981, Ann. Nucl. Energy, 8, 657
Nordland, A. 1991, in Stellar Atmospheres: Beyond Classical Models, ed. L. Crivellari, I. Hubeny, & D. G. Hummer (Dordrecht: Kluwer), 61
Olson, G. L., Auer, L. H., & Buchler, J. R. 1986, J. Quant. Spectrosc. Radiat. Transfer, 35, 431
Reed, W. H., & Hill, T. R. 1973, paper presented at meeting of the American Nuclear Society, Ann Arbor
Rybicki, G. 1971, J. Quant. Spectrosc. Radiat. Transfer, 11, 589